# Tracer transport within abyssal mixing layers

Ryan M. Holmes, Casimir de Lavergne, Trevor J. Mcdougall

# Tracer transport within abyssal mixing layers

R. M. Holmes*

*School of Mathematics and Statistics, Climate Change Research Centre and the Australian Research Council Centre of Excellence for Climate Extremes, University of New South Wales, Sydney, NSW, Australia*

Casimir de Lavergne† and Trevor J. McDougall

*School of Mathematics and Statistics, University of New South Wales, Sydney, NSW, Australia*

*Corresponding author address:* School of Mathematics and Statistics, University of New South Wales, Sydney, Australia

E-mail: ryan.holmes@unsw.edu.au

†Current affiliation: LOCEAN Laboratory, Sorbonne Université-CNRS-IRD-MNHN, Paris, France

## ABSTRACT

Mixing layers near sloped topography in the abyss are thought to play a critical role in the global overturning circulation. Yet the behavior of passive tracers within sloping boundary layer systems has received little attention, despite the extensive use of tracer observations to understand abyssal circulation. Here, we investigate the behavior of a passive tracer released near a sloping boundary within a flow governed by one-dimensional boundary layer theory. The spreading rate of the tracer across isopycnals is influenced by a number of factors including the bottom-intensification of mixing, the dipole of upwelling (in the boundary layer) and downwelling (in the outer mixing layer) and along-isopycnal diffusion. For isolated near-boundary tracer releases the bulk diffusivity, proportional to the rate of increase of the variance of the tracer distribution in buoyancy space, is much less than what would be expected from averaging the diapycnal diffusivity over the tracer patch. This stems from the presence of the bottom boundary that prevents tracer diffusion through it. Furthermore, when along-isopycnal diffusion is weak, the boundary tends to drive the tracer up the slope toward less dense fluid on average due to asymmetries between boundary layer and interior flows. With strong along-isopycnal diffusion this upslope movement is reduced, while at the same time the average diapycnal spreading rate is increased due to a reduced influence of the bottom boundary. These results have implications for what can be learned about the characteristics of mixing near sloping boundaries from past and future tracer-release experiments.

## 1. Introduction

The transport of tracers within the ocean plays an important role not only in ocean dynamics, thermodynamics and biogeochemistry, but also as a method with which to observe the ocean, and infer circulation properties. Because, by its nature, tracer transport integrates over both spatial and temporal scales, it allows us to measure the large-scale, integral impact of a range of smaller scale processes that are difficult to observe directly. However, in order to correctly interpret and use tracer measurements, a good understanding of tracer transport and its relation to circulation properties is needed.

Tracer transport has been particularly useful for understanding the dynamics of the ocean's deep overturning circulation, where small-scale turbulent mixing plays a key role (Watson and Ledwell 2000). Since the pioneering study of Munk (1966) and the realization that mixing in the interior is generally weak (e.g. Ledwell et al. 1993), mixing near the ocean's boundaries has been thought to play a critical role in closing the global diapycnal circulation (Armi 1978; Ivey 1987b; Wunsch 1970; Phillips 1970; Thorpe 1987; Garrett 1991). Observations suggest that turbulent mixing is bottom intensified due to internal wave breaking within the stratified fluid above the boundary layer (Toole et al. 1994; Polzin et al. 1997; Ledwell et al. 2000; St. Laurent et al. 2012; Waterhouse et al. 2014). The bottom-intensification of mixing within so called "abyssal mixing layers" implies a downward mass transport across isopycnals in what some authors have termed the Stratified Mixing Layer (SML, McDougall and Ferrari 2017). In order to balance the formation of dense waters at high-latitudes there must therefore be a somewhat larger upwelling transport within thin bottom boundary layers (BBLs) along the sloping seafloor where the turbulent buoyancy flux converges (de Lavergne et al. 2016, 2017; Ferrari et al. 2016; McDougall and Ferrari 2017). The requirement for net upwelling and the near-compensation between the net diapycnal transports

in the BBL and SML imply a complex balance between factors such as topographic geometry (McDougall and Ferrari 2017; Holmes et al. 2018), variations in stratification (Ferrari et al. 2016; Callies and Ferrari 2018; Banyte et al. 2018) and the lateral structure in the intensity of turbulent mixing near the ocean floor (Kunze 2017a,b). How this balance is achieved at both global and regional scales remains an open question that observations of tracer behavior may help to answer.

Field tracer release experiments (TREs) have provided many insights into the dynamics of diapycnal ocean circulation. TREs have shown that mixing away from boundaries is weak (Ledwell et al. 1993; Ledwell 1998), and highlighted the importance of strong boundary mixing for closing basin-scale budgets (Goudsmit et al. 1997; Inall 2009; Ledwell and Bratkovich 1995). The Brazil Basin TRE (BBTRE, Ledwell et al. 2000) in particular demonstrated the presence of intensified mixing in the abyss above the rough seafloor of the Mid-Atlantic Ridge, corroborating microstructure measurements (Polzin et al. 1997). The BBTRE tracer was released well above the ocean bottom, and its centroid showed a tendency to descend across isopycnals in the eastern basin consistent with the expected diapycnal downwelling in the SML. However, the observations close to the boundary suggested that in ridge canyons the tracer moves upslope, likely toward less dense waters. These observations pointed to the importance of the near boundary region, though BBTRE was not designed to study this region.

The importance of intense boundary mixing was further highlighted by the Diapycnal and Isopycnal Mixing Experiment in the Southern Ocean (DIMES, Ledwell et al. 2011; Watson et al. 2013). DIMES also exposed a common discrepancy whereby diffusivities inferred from tracer measurements often exceed those estimated from microstructure surveys. These discrepancies are often attributed to sampling issues (e.g. Wüest et al. 1996; Voet et al. 2015) and can be reconciled if the full temporal and spatial distribution of the tracer is taken into account (Mashayek et al. 2017). Studies such as Mashayek et al. (2017) and Ledwell et al. (2000) highlight the importance of

tracer-boundary interactions, but do not discuss the details of tracer transport within any particular boundary-driven flow. Idealized studies have examined near-boundary tracer dispersion above a horizontal boundary (e.g. Saffman 1962; Csanady 1969). Here we examine a similar problem near a sloping boundary.

Our tracer study will be conducted in the context of one-dimensional boundary layer theory (e.g. Wunsch 1970; Phillips et al. 1986; Thorpe 1987; Garrett 1990). The theory considers the one-dimensional problem of flow over a uniform slope driven by an isotropic diffusivity. To satisfy the no-flux boundary condition, isopycnals slope down as they approach the boundary, leading to a buoyancy-driven upslope flow in a weakly-stratified BBL where friction is important (Garrett et al. 1993). When the diffusivity is bottom-intensified a corresponding downslope flow appears in the outer portion of the abyssal mixing layer (the SML). Recently, Callies (2018) has shown that for realistic abyssal ocean parameters boundary layer theory predicts a much weaker stratification than typically observed. He suggests that restratification by submesoscale eddies, generated by baroclinic instability of the resulting flow field (Wenegrat et al. 2018), is necessary to maintain the stratification and therefore permit significant near-boundary water-mass transformation.

Eddies, along with tides, intrusions and other processes, can also drive strong along-isopycnal tracer transports (e.g. Ivey 1987a; McPhee-Shaw 2006; Wain and Rehmann 2010; Winters 2015; Dell and Pratt 2015). This along-isopycnal exchange (in this article captured at first-order by an along-isopycnal tracer diffusivity) provides one means in which the strong boundary mixing can communicate with the interior.

In this article we will aim to address the following questions; 1) what processes within abyssal mixing layers are most important for determining tracer transport? 2) Will a tracer be transported toward lighter (upslope) or heavier (downslope) density classes, on average, when released near

a sloping boundary? 3) What can be inferred about the properties of mixing and circulation from bulk measurements of the tracer cloud dispersion?

To approach these questions we analyze the behavior of a passive tracer released within a flow governed by one-dimensional boundary layer theory (described in Section 2). The tracer evolves in two dimensions due to the effects of diapycnal diffusion, isopycnal diffusion and advection (Section 3). We introduce an analytical framework based around the tracer moments in buoyancy space (the tracer center-of-mass and variance) to understand the contribution of different processes to tracer dispersion (Sections 4-6). We find that the presence of the boundary can slow the rate of diapycnal tracer dispersion below that expected from averaging the diapycnal diffusivity over the tracer patch. Due to asymmetries between the upslope BBL and downslope SML flows (the BBL upwelling being strong and narrow compared to the more diffuse SML downwelling), the tracer tends to move upslope on average. The extent of upslope movement and tracer dispersion depends on the initial release position of the tracer, as well as a number of other factors such as the decay scale of bottom-intensified mixing and along-isopycnal diffusion (Section 7). Our results have implications not only for our understanding of tracer behavior near the ocean floor (Section 9), but also for what can be learned about ocean dynamics from field TREs (Section 8).

## 2. Boundary layer theory

The idealized two-dimensional tracer release experiments will be performed within a flow governed by one-dimensional boundary layer theory. In this section we briefly review the key results required for our tracer study. For a more detailed derivation the reader is referred to Garrett (1990, 1991) and Callies (2018). We consider steady flow above a bottom with uniform slope $\tan\theta$ and use a coordinate system aligned with the bottom (i.e. $z$ is bottom-normal with origin at the boundary, $y$ is upslope and $x$ is along-slope, Fig. 1). Everything is uniform in the upslope and along-slope

directions except pressure and buoyancy (and in the next section the tracer). Buoyancy is characterized by a constant far-field vertical stratification $N^2$,

$$\frac{\partial b}{\partial z} \to N^2 \cos\theta, \quad \text{as} \quad z \to \infty \tag{1}$$

$$\frac{\partial b}{\partial y} = N^2 \sin\theta, \quad \text{all } z, \tag{2}$$

where $b$ is the buoyancy field relative to a reference density $\rho_0$. The steady, rotating equations of motion for this system are (e.g. Garrett et al. 1993),

$$-fV\cos\theta = \frac{d}{dz}\left(\nu_u \frac{dU}{dz}\right), \tag{3}$$

$$fU\cos\theta = -\frac{1}{\rho_0}\frac{\partial P}{\partial y} + b\sin\theta + \frac{d}{dz}\left(\nu_v \frac{dV}{dz}\right), \tag{4}$$

$$0 = -\frac{1}{\rho_0}\frac{\partial P}{\partial z} + b\cos\theta, \tag{5}$$

$$N^2 V \sin\theta = \frac{d}{dz}\left(\kappa \frac{\partial b}{\partial z}\right), \tag{6}$$

where $U(z), V(z)$ are the along-slope and upslope velocities, $\nu_u(z), \nu_v(z)$ are along-slope and upslope eddy viscosities (which may differ for reasons discussed shortly), $\kappa(z)$ is an eddy diffusivity, $P(y,z)$ is the pressure field and $f$ is the (vertical) Coriolis parameter. These equations can be combined into (e.g. Garrett 1991),

$$\frac{d^2}{dz^2}\left(\nu_v \frac{d^2\Psi}{dz^2}\right) + \left(\frac{f^2\cos^2\theta}{\nu_u} + \frac{N^2\sin^2\theta}{\kappa}\right)\Psi = N^2\sin\theta\cos\theta + \frac{f^2\cos^2\theta}{\nu_u}\kappa_\infty\cot\theta, \tag{7}$$

where $\kappa_\infty$ is the far-field diffusivity and the scalar streamfunction $\Psi(z)$ is given by $\frac{d\Psi}{dz} = V$ with $\Psi(0) = 0$ and,

$$\Psi \to \kappa_\infty \cot\theta, \quad \text{as} \quad z \to \infty. \tag{8}$$

For constant diffusion, $\nu_u(z) = \nu_{u0}$, $\nu_v(z) = \nu_{v0}$, $\kappa(z) = \kappa_0$ $(= \kappa_\infty)$, the solution with no-slip boundary conditions is characterized by a BBL of reduced stratification and upslope flow (Wunsch 1970; Thorpe 1987, dashed black lines in Fig. 2). There is an along-slope flow in the interior in the

direction opposite to Kelvin wave propagation, or upwelling-favorable in a bottom-Ekman sense (Garrett et al. 1993). The BBL width is $\mathscr{O}(q_0^{-1})$ where,

$$q_0^4 = \frac{N^2 \sin^2\theta}{4Pr_{v0}\kappa_0^2}\left(1 + (SPr_{u0})^{-1}\right), \tag{9}$$

$S^{-1} = f^2\cos^2\theta/N^2\sin^2\theta$ is the inverse slope Burger number and $Pr_{u0} = \nu_{u0}/\kappa_0$, $Pr_{v0} = \nu_{v0}/\kappa_0$ are Prandtl numbers. For typical abyssal parameters of $N^2 = 10^{-6}\mathrm{s}^{-2}$, $f = 10^{-4}\mathrm{s}^{-1}$, $\nu_{u0} = \nu_{v0} = \kappa_0 = 10^{-3}\mathrm{m}^2\mathrm{s}^{-1}$, $\tan\theta = 1/400$ then $S^{-1} = 1600$ is large and the BBL thickness corresponds to an Ekman layer thickness of $q_0^{-1} = 4.5\mathrm{m}$.

In this article we will instead focus on the case where the diffusivity is bottom intensified with form,

$$\kappa = \kappa_\infty + (\kappa_0 - \kappa_\infty)e^{-z/d}, \tag{10}$$

where $\kappa_0$ is the diffusivity near the boundary and $d$ is a decay scale. For the parameter space of interest here the BBL thickness $q_0^{-1}$ is much smaller than the diffusivity decay scale $d$. Following Callies (2018), for $q_0 d >> 1$ we can construct an approximate analytic solution for the bottom-intensified case by patching together a solution in the BBL, where the mixing coefficients can be assumed to be constant and equal to their near-boundary values $\nu_{u0}$, $\nu_{v0}$ and $\kappa_0$, to a solution in the interior, where the influence of friction through the fourth derivative term in Eq. (7) can be neglected. This procedure is presented in Appendix A.

However, as shown by Callies (2018) (see Eqs. (68) and (71) in Appendix A), for the typical large inverse slope Burger number $S^{-1}$ and order one Prandtl number regime in the abyssal ocean such a solution predicts very weak stratification over the abyssal mixing layer. Callies (2018) attributes this weak stratification to the lack of representation of baroclinic instability and its associated eddy-driven restratification in the one-dimensional system. A realistically stratified one-dimensional solution requires small values of the parameter $(SPr_{u0})^{-1}$ (see Appendix A for

more details) and can therefore be recovered using a large $Pr_{u0}$. Such a choice of large vertical momentum mixing in the along-slope momentum equation can be physically interpreted as a parameterization for restratification by baroclinic eddies based on the thickness-weighted average formalism (Rhines and Young 1982; Greatbatch and Lamb 1990; Gent and McWilliams 1990; Gent et al. 1995). For simplicity, and to avoid the need to resolve eddies or include an explicit Gent and McWilliams (1990) type parameterization, throughout most of this article we will consider the limit $(SPr_{u0})^{-1} \to 0$ obtained for large $Pr_{u0}$. This choice assumes that eddies maintain the stratification in the SML at its far-field value[1]. In Section 7c we briefly discuss the impact of reduced stratification in the SML through a non-zero $(SPr_{u0})^{-1}$.

Note that the representation of eddy-driven restratification through enhanced vertical momentum mixing should have less impact on the BBL solution, which is determined by non-geostrophic frictional turbulent boundary layer physics. The eddy-driven restratification and frictional boundary layer processes can be conveniently isolated (at least in our two-dimensional context) by enhancing only the along-slope viscosity. Thus we maintain the choice $Pr_{v0} = 1$ in the upslope momentum equation.

With these parameter choices, the full one-dimensional solution is given by (taking the limit $(SPr_{u0})^{-1} \to 0$ in Eqs. (68) and (71) in Appendix A),

$$\Psi = \kappa \cot\theta \left(1 - e^{-q_0 z}\left(\cos q_0 z + \sin q_0 z\right)\right), \tag{11}$$

$$\frac{\partial b}{\partial z} = N^2 \cos\theta \left(1 - e^{-q_0 z}\left(\cos q_0 z + \sin q_0 z\right)\right). \tag{12}$$

As for a constant $\kappa$ solution there is a BBL of thickness $\sim q_0^{-1}$ with weak stratification and upslope flow (solid lines with circles in Fig. 2)[2]. Outside the BBL the vertical stratification is equal to the

[1]This parameter choice is equivalent to using non-rotating boundary layer theory due to the parameter dependence $(SPr_{u0})^{-1} \sim f^2/\nu_{u0}$.

[2]Note that due to the choice $(SPr_{u0})^{-1} \to 0$ the BBL thickness is modestly increased to $q_0^{-1} \sim 28$m for the typical abyssal parameters considered above.

far-field value $N^2$ and there is a weak downslope flow which largely compensates the upwelling within the BBL (the imbalance between SML and BBL transports is governed by Eq. (8)). These compensating upwelling and downwelling flows are equivalent to the water-mass transformation dipole discussed recently by a number of authors (e.g. de Lavergne et al. 2016; Ferrari et al. 2016; McDougall and Ferrari 2017). It is this flow that will be used to advect and diffuse a passive tracer in a two-dimensional $y$-$z$ plane, as discussed in the next section.

## 3. Two-dimensional tracer dispersion in a one-dimensional slope flow

### *a. The tracer conservation equation*

We set up a two-dimensional tracer advection-diffusion problem in the one-dimensional boundary layer flow discussed in the previous section. That is, we look for the distribution of a tracer $\mathcal{C}(y,z,t)$ (where $\mathcal{C}$ has concentration units of tracer m$^{-2}$) which varies in the upslope and slope-normal directions (Fig. 1) given an initial distribution $\mathcal{C}(y,z,0)$ and a tracer conservation equation,

$$\frac{\partial \mathcal{C}}{\partial t} = -\nabla \cdot \boldsymbol{F}_{\mathcal{C}}, \tag{13}$$

where the tracer flux,

$$\boldsymbol{F}_{\mathcal{C}} = \boldsymbol{V}\mathcal{C} - \kappa \nabla \mathcal{C} - A_H \boldsymbol{K}_I \cdot \nabla \mathcal{C}. \tag{14}$$

$\boldsymbol{F}_{\mathcal{C}}$ has three-components; an advective flux associated with the velocity $\boldsymbol{V} = (V(z),0)$ from boundary layer theory ($V(z)$ is given by the $z$ derivative of Eq. (11)) and diffusive fluxes associated with a small-scale isotropic diffusivity $\kappa(z)$ and an along-isopycnal diffusivity $A_H$. The along-isopycnal diffusion is specified using the symmetric second rank tensor (Redi 1982),

$$\boldsymbol{K}_I = \frac{1}{|\nabla b|^2} \begin{bmatrix} b_z^2 & -b_y b_z \\ -b_y b_z & b_y^2 \end{bmatrix}, \tag{15}$$

where the subscript on $b$ indicates differentiation. The coefficients of $\boldsymbol{K}_I$ are determined using the buoyancy gradients $b_z = B_z + b'_z = N^2\cos\theta + b'_z$ and $b_y = B_y = N^2\sin\theta$ split into background ($B_z$ and $B_y$) and perturbation components where from Eq. (12),

$$b'_z = -N^2\cos\theta e^{-q_0 z}\left(\cos q_0 z + \sin q_0 z\right). \tag{16}$$

This formulation of the tracer equation is consistent with boundary layer theory (i.e. if $b$ replaces $\mathcal{C}$ then Eq. (13) reduces to Eq. (6)).

*b. Numerical model setup*

The tracer conservation Eq. (13) cannot be solved analytically in the general case (although we will consider simplified cases that can be solved analytically) and so we resort to numerical simulations. We use the spectral code Dedalus (Burns et al. 2019, http://dedalus-project.org/) in the rotated $y,z$ coordinates (Fig. 1) with periodic boundary conditions in $y$. We consider a control parameter set with a $y$-domain length $L_y = 1500$km, a slope of $\alpha = 1/400$ (roughly the western side of the Mid-Atlantic Ridge) and a $z$-domain height of $L_z = 3000$m. The far-field stratification $N^2 = 10^{-6}\mathrm{m^2 s^{-1}}$. The diffusivity will either be bottom-intensified with an exponential profile [Eq. (10)] or constant, with base parameters $d = 500$m, $\kappa_0 = 10^{-3}\mathrm{m^2 s^{-1}}$ and $\kappa_\infty = 10^{-5}\mathrm{m^2 s^{-1}}$. For those simulations with no along-isopycnal diffusion ($A_H = 0$) we use 384 Fourier modes in $y$ and 192 Chebyshev modes in $z$, corresponding to an average $\Delta y \sim 4$km and an average $\Delta z = 15$m. The Chebyshev basis allows finer resolution of the small-scale $z$ gradients in the BBL (see Fig. 2). Eq. (13) is solved implicitly in time using a time step of 8 days. However, because of small-scale variations in the along-isopycnal tensor coefficients [Eq. (15)] near the boundary, those simulations with non-zero along-isopycnal diffusion were instead performed with 576 modes in $y$ and 768 modes in $z$ and a time step of 4 days. The simulations match analytic results almost

perfectly where such results are obtainable (e.g. Section 5). The results are robust to numerical choices, as confirmed by doubling the number of modes in $z$ and running with a time step four times smaller, which gave almost identical results (not shown).

## 4. Bulk diffusivity and tracer moments

The simplest and most common method to quantify the overall tracer dispersion rate in different coordinates is through the rate of increase of the variance of the tracer distribution. A Gaussian distribution of tracer spreading in one-dimension ($s$) due to a constant diffusivity $\kappa$ evolves as,

$$\mathcal{C}(s,t) = A\frac{\sigma_0}{\sigma}e^{-(s-\mu)^2/2\sigma^2}, \tag{17}$$

$$\sigma^2(t) = \sigma_0^2 + 2\kappa t, \tag{18}$$

where $t$ is time, $A$ is a constant, $\sigma^2$ is the variance with initial value $\sigma_0^2$ and $\mu$ is the centroid or center-of-mass. The variance increases linearly with time at a rate of $2\kappa$. Thus for any tracer distribution, which may be spreading due to complex advection-diffusion processes in multiple dimensions, we can define an equivalent or *bulk diffusivity* in any dimension $s$ in terms of the rate of increase of the variance $\sigma_s$ (also see Wüest et al. 1996; Goudsmit et al. 1997),

$$\kappa_{bk}^s = \frac{1}{2}\frac{\partial\sigma_s^2}{\partial t}. \tag{19}$$

Here, by defining a domain averaging operator over the dimension $s$,

$$\langle * \rangle^s \equiv \int_{-\infty}^{\infty} * \, ds, \tag{20}$$

we can write both the variance $\sigma_s$ and the center-of-mass $\mu_s$ in terms of the *s-moments* of the tracer distribution,

$$\mu_s \equiv \frac{\langle s\mathcal{C}\rangle^s}{\langle\mathcal{C}\rangle^s}, \tag{21}$$

$$\sigma_s^2 \equiv \frac{\langle s^2\mathcal{C}\rangle^s}{\langle\mathcal{C}\rangle^s} - \mu_s^2, \tag{22}$$

where $\langle s\mathcal{C}\rangle^s$ and $\langle s^2\mathcal{C}\rangle^s$ are the first and second moments, and $\langle\mathcal{C}\rangle^s = A\sqrt{2\pi}\sigma_s$ is the zeroth moment that quantifies the (conserved) total amount of tracer. The moments provide a useful framework that can be used to understand aspects of the tracer dispersion analytically (e.g., Saffman 1962; Young et al. 1982). They will be used in later sections to derive expressions for the evolution of the tracer center-of-mass and bulk diffusivity in terms of the various advective and diffusive tracer fluxes.

A similar calculation can also be applied in buoyancy space, to obtain a *bulk diapycnal diffusivity* $\kappa^b_{bk}$ (or just $\kappa_{bk}$). In this case a mean stratification profile $N^2$, which in our two-dimensional context will be the interior stratification which (in the limit $(SPr_{u0})^{-1} \to 0$) is independent of height and time, is also required in order to convert the spreading rate into the units of a diffusivity. We define,

$$\kappa_{bk} \equiv \frac{1}{N^4}\frac{1}{2}\frac{\partial\sigma_b^2}{\partial t} \tag{23}$$

where,

$$\mu_b = \frac{\langle b\mathcal{C}\rangle}{\langle\mathcal{C}\rangle}, \tag{24}$$

$$\sigma_b^2 = \frac{\langle b^2\mathcal{C}\rangle}{\langle\mathcal{C}\rangle} - \mu_b^2, \tag{25}$$

and the averaging operation in our general two-dimensional context occurs over the full tracer distribution in the two spatial dimensions $y$ and $z$,

$$\langle * \rangle \equiv \langle\langle * \rangle^y\rangle^z = \int_0^\infty \int_{-\infty}^\infty * \, dydz. \tag{26}$$

The bulk diffusivity [Eq. (23)] will be used to characterize the overall rate of spreading of the tracer across buoyancy surfaces. However, it should be emphasized that $\kappa_{bk}$ should not necessarily be interpreted directly as a diffusivity, as such an interpretation masks the potentially complex processes that are leading to the spreading of that tracer distribution in the first place (here, two-dimensional advection and diffusion). Comparisons of $\kappa_{bk}$ to the actual isotropic diffusivity $\kappa$

will prove useful, as is commonly done for field TREs where microstructure measurements are also available (e.g. Ledwell et al. 2000; Watson et al. 2013; Mashayek et al. 2017). We will also compare $\kappa_{bk}$ to the diffusivity calculated using a one-dimensional model commonly applied to field data (Ledwell and Watson 1991; Ledwell 1998, see Appendix B).

## 5. Boundary restriction: tracer behavior in $z$

We begin by examining the behavior of the tracer in the slope-normal coordinate $z$. Integrating the two-dimensional tracer conservation equation [Eq. (13)] across all $y$ yields,

$$\frac{\partial \langle \mathcal{C} \rangle^y}{\partial t} = \frac{\partial}{\partial z}\left( K^z \frac{\partial \langle \mathcal{C} \rangle^y}{\partial z} \right), \tag{27}$$

where $K^z = \kappa + A_H b_y^2/|\nabla b|^2$ and the boundary conditions are $K^z \frac{\partial \langle \mathcal{C} \rangle^y}{\partial z} = 0$ at $z = 0$ and $\langle \mathcal{C} \rangle^y \to 0$ as $z \to \infty$. Thus in the slope-normal coordinate $z$ the tracer diffuses according to a one-dimensional diffusion equation that does not depend on the upslope velocity $V$. We are not aware of any analytic solutions to Eq. (27) for the case where $\kappa$ is exponential, $A_H$ is non-zero and there is a boundary at $z = 0$ (see Zamani and Bombardelli 2014, and references therein). However, when $K^z$ is a constant (where here for simplicity we set $K^z = \kappa$ with $\kappa$ constant) a solution is easy to obtain and, despite the simple governing equation, shows some interesting behavior as a consequence of the boundary at $z = 0$.

### *a. Constant diffusivity*

When $\kappa$ is constant and $A_H = 0$ the tracer evolution for an initial Gaussian distribution with center-of-mass at $z = \mu_0$ and spread $\sigma_0$ (provided the initial tracer distribution is isolated from the

boundary, $\sigma_0 << \mu_0$) is given by the sum of two Gaussians centered at $z = \mu_0$ and $z = -\mu_0$,

$$\langle \mathcal{C} \rangle^y(z,t) = A\frac{\sigma_0}{\sigma}\left(e^{-(z-\mu_0)^2/2\sigma^2} + e^{-(z+\mu_0)^2/2\sigma^2}\right), \tag{28}$$

$$\text{where} \quad \sigma^2(t) = \sigma_0^2 + 2\kappa t. \tag{29}$$

Due to the symmetry about $z = 0$, this solution satisfies the no flux boundary condition at $z = 0$, while the individual Gaussians satisfy the one-dimensional diffusion equation without a boundary. This analytic solution matches the numerical two-dimensional solution averaged in $y$ (shown at three different times by the orange curves in Fig. 3a).

The center-of-mass, variance and bulk diffusivity derived from the $z$-moments of this solution (defined for $z > 0$ using Eq. (26) for the domain average) are,

$$\mu_z = \frac{\langle z\mathcal{C} \rangle}{\langle \mathcal{C} \rangle} = \frac{2\sigma}{\sqrt{2\pi}}e^{-\mu_0^2/2\sigma^2} + \mu_0 \text{Erf}(\frac{\mu_0}{\sqrt{2\sigma^2}}) \tag{30}$$

$$\sigma_z^2 = \frac{\langle z^2\mathcal{C} \rangle}{\langle \mathcal{C} \rangle} = \mu_0^2 + \sigma^2 - \mu_z^2 \tag{31}$$

$$\kappa_{bk}^z = \frac{1}{2}\frac{\partial \sigma_z^2}{\partial t}$$

$$= \kappa\left(1 - \frac{2}{\pi}e^{-\mu_0^2/\sigma^2} - \frac{2\mu_0}{\sqrt{2\pi\sigma^2}}\text{Erf}(\frac{\mu_0}{\sqrt{2\sigma^2}})e^{-\mu_0^2/2\sigma^2}\right) \tag{32}$$

At early times, when $\mu_z >> \sigma$ the center-of-mass is stationary $\mu_z = \mu_0$, $\sigma_z^2 = \sigma^2$ and the bulk diffusivity is equal to the actual diffusivity $\kappa_{bk}^z = \kappa$. However, as time increases, namely once the tracer encounters the boundary such that $\sigma \sim \mu_z$, the center-of-mass moves away from the boundary, eventually increasing like the square-root of time $\mu_z \sim \sqrt{t}$ (orange line in Fig. 3b). As a result, the rate of increase of variance $\sigma_z$ reduces (due to the $\mu_z^2$ term in Eq. (31), orange line in Fig. 3c), and the bulk diffusivity is reduced below $\kappa$ (compare orange solid and dashed lines in Fig. 3c). Hence the effect of the boundary is to reduce the bulk diffusivity by limiting downward tracer spreading. In the limit of long time,

$$\kappa_{bk}^z \to (1 - \frac{2}{\pi})\kappa \approx 0.36\kappa, \quad \text{as} \quad t \to \infty, \tag{33}$$

meaning that the bulk diffusivity is reduced by more than a factor of two. This is perhaps surprising, since it may be thought that the boundary prevents the spreading of half of the Gaussian tracer distribution. However, once the tracer encounters the boundary it no longer spreads like a half-Gaussian because its 'reflection spreads into the region $z > 0$, resulting in an effective accumulation of tracer near the boundary.

*b. Bottom-intensified diffusivity*

When instead the diffusivity is bottom intensified ($\kappa_\infty \neq \kappa_0$, with $A_H = 0$) the solution cannot be obtained analytically. However, the influence of the boundary on the tracer diffusion can still be understood by deriving equations for the evolution of the $z$-moments directly from the tracer conservation equation (this technique will also be used in later sections to analyze the tracer behavior in buoyancy coordinates). Multiplying Eq. (27) by $z$ and integrating over the domain,

$$\langle \mathcal{C} \rangle \frac{\partial \mu_z}{\partial t} = \frac{\partial \langle z\mathcal{C} \rangle}{\partial t} = \langle z \frac{\partial}{\partial z} (\kappa \mathcal{C}_z) \rangle, \tag{34}$$

$$= \langle \frac{\partial}{\partial z} (z\kappa \mathcal{C}_z) \rangle + \langle -\kappa \mathcal{C}_z \rangle \tag{35}$$

$$= \langle -\kappa \mathcal{C}_z \rangle, \tag{36}$$

where in the second line we have used the chain rule and the third line we have used the boundary condition at $z = 0$ to eliminate the first term. Eq. (36) simply states that the tracer center-of-mass will move according to the domain-averaged tracer flux. Furthermore, using the chain rule to move the $z$-derivative from $\mathcal{C}$ to $\kappa$ and the boundary condition to rewrite $\langle \partial_z(\kappa \mathcal{C}) \rangle$ in terms of the tracer concentration on the boundary yields,

$$\langle \mathcal{C} \rangle \frac{\partial \mu_z}{\partial t} = \kappa_0 \int_{-\infty}^{\infty} \mathcal{C}(y, 0, t) dy + \langle \kappa_z \mathcal{C} \rangle. \tag{37}$$

The first term in Eq. (37) exposes the "boundary effect" discussed above: the boundary prevents the tracer flux in the negative $z$ direction (once tracer accumulates there) and thus the flux in the

positive $z$ direction dominates, driving the center-of-mass away from the boundary. A $z$-dependent diffusivity can also drive net tracer movement through the second term in Eq. (37). For a bottom-intensified diffusivity, this term enhances the downward tracer diffusion below the initial tracer patch driving the center-of-mass toward the boundary (dotted blue line in Fig. 3b). However, this downward motion is transient and the boundary effect dominates once enough tracer accumulates on the boundary (solid blue line in Fig. 3b).

An equation for the second $z$ tracer moment can be derived using a procedure analogous to that employed for Eq. (36),

$$\frac{\partial \langle z^2 \mathcal{C} \rangle}{\partial t} = 2\langle -\kappa \mathcal{C}_z z \rangle. \tag{38}$$

The bulk diffusivity or rate of change of the variance is then,

$$\kappa^z_{bk} = \frac{\langle -\kappa \mathcal{C}_z (z-\mu_z) \rangle}{\langle \mathcal{C} \rangle}, \tag{39}$$

I.e. $\kappa^z_{bk}$ is given by the domain-averaged tracer fluxes weighted by their distance from the center-of-mass $z-\mu_z$. Furthermore, by shifting the $z$-derivative from the $\mathcal{C}$ to $\kappa$, and absorbing the factor $(z-\mu_z)$,

$$\kappa^z_{bk} = \frac{\langle \kappa \mathcal{C} \rangle}{\langle \mathcal{C} \rangle} - \frac{\mu_z \kappa_0}{\langle \mathcal{C} \rangle} \int_{-\infty}^{\infty} \mathcal{C}(y,0,t)dy + \frac{\langle (z-\mu_z)\mathcal{C}\kappa_z \rangle}{\langle \mathcal{C} \rangle}. \tag{40}$$

Eq. (40) clearly shows that the bulk diffusivity $\kappa^z_{bk}$ is not what would be expected from simply averaging the isotropic diffusivity $\kappa$ over the tracer patch (or the *in-situ diffusivity* $\langle \kappa \mathcal{C} \rangle / \langle \mathcal{C} \rangle$, dashed lines in Fig. 3c, also see Mashayek et al. 2017). Instead, the boundary significantly *reduces* this spreading rate, once tracer encounters the boundary (compare solid and dashed lines in Fig. 3c). This occurs because the boundary prevents tracer spreading in the negative $z$ direction, and constricts the tracer to remain closer to its center-of-mass [Eq. (39)]. On the other hand, the vertical diffusivity gradient, when present, drives a modest enhancement of the bulk diffusivity

through the last term in Eq. (40) (dotted blue line in Fig. 3c). It should be noted that the terms in Eq. (40) [and Eq. (37)] are not independent; each term affects the tracer distribution $\mathcal{C}$ on which they are all dependent.

## 6. Diapycnal spreading: tracer behavior in $b$

Though the upslope velocity $V$ does not influence the spreading of the tracer in the slope normal direction $z$, it does affect the tracer spreading rate in the upslope direction $y$ and across buoyancy surfaces. The two-dimensional evolution of tracer patches released at $z_0 = d/2 = 250$m in flows with constant (Fig. 4a-c) and bottom-intensified (Fig. 4d-f) diffusivities clearly show the impacts of the boundary layer flow. With a constant diffusivity there is only upslope flow within the BBL. This flow drives tracer up the slope after which it diffuses vertically out of the BBL, forming a characteristic upslope tracer tongue (Fig. 4a-c). The center-of-mass (with upslope position $\mu_y = \langle y\mathcal{C}\rangle/\langle\mathcal{C}\rangle$) moves up the slope, at a rate determined by the tracer-weighted velocity,

$$\frac{\partial \mu_y}{\partial t} = \frac{\langle V\mathcal{C}\rangle}{\langle\mathcal{C}\rangle}, \tag{41}$$

(obtained by multiplying Eq. (13) by $y$ and integrating over the domain), and slightly away from the boundary ($\mu_z$ increases, see closed circles in Fig. 4a-c). Thus the advective tracer transport in the BBL is significant despite its thinness. The expanding tracer patch continues to supply tracer to the BBL through downward diffusion, accounting for the large-amount of tracer advected upward within the BBL.

When the diffusivity is instead bottom-intensified (Fig. 4d-f), the upslope spreading of tracer is reduced due to both the restriction of diffusion to the region near the boundary and the presence of downslope transport in the SML (compare closed circles in Figs. 4c and 4f). Due to the shear in the SML velocity, the expanding interior tracer patch acquires a tilt.

The evolution of the tracer concentrations binned into buoyancy classes also indicates a strong upward net motion of the tracer distribution, in both cases (orange and blue distributions in Fig. 5a), reflected in the upward motion of the center-of-mass (solid lines in Fig. 5b). In the following subsections we develop a framework based on the tracer moments to evaluate the contributions of various advective and diffusive tracer fluxes to the diapycnal tracer spreading.

*a. Advective and diffusive tracer fluxes and the buoyancy budget constraint*

Following the same procedure used in Section 5 for the one-dimensional case, we obtain the following equations for the buoyancy-moments of the tracer,

$$\frac{\partial \langle b\mathcal{C}\rangle}{\partial t} = \langle \boldsymbol{F}_{\mathcal{C}} \cdot \nabla b\rangle, \tag{42}$$

$$\frac{\partial \langle b^2\mathcal{C}\rangle}{\partial t} = 2\langle b\boldsymbol{F}_{\mathcal{C}} \cdot \nabla b\rangle, \tag{43}$$

$$\kappa_{bk} = \frac{1}{N^2\langle \mathcal{C}\rangle}\langle (b-\mu_b)\boldsymbol{F}_{\mathcal{C}} \cdot \nabla b\rangle, \tag{44}$$

where $\mu_b = \langle b\mathcal{C}\rangle/\langle \mathcal{C}\rangle$. Eq. (42) shows that the tracer center-of-mass moves across isopycnals if the domain-averaged diapycnal tracer flux is non-zero. The rate of change of the tracer variance in buoyancy space, proportional to $\kappa_{bk}$ [Eq. (44)], is positive if the diapycnal fluxes move tracer on average away from the tracer center-of-mass $\mu_b$. Noting that the along-isopycnal flux drops out yields contributions from diapycnal advection and isotropic diffusion,

$$\frac{\partial \langle b\mathcal{C}\rangle}{\partial t} = \langle \mathcal{C}\boldsymbol{V} \cdot \nabla b\rangle - \langle \kappa \nabla \mathcal{C} \cdot \nabla b\rangle, \tag{45}$$

$$\kappa_{bk} = \frac{1}{N^4\langle \mathcal{C}\rangle}\langle (b-\mu_b)\mathcal{C}\boldsymbol{V} \cdot \nabla b\rangle - \frac{1}{N^4\langle \mathcal{C}\rangle}\langle (b-\mu_b)\kappa \nabla \mathcal{C} \cdot \nabla b\rangle. \tag{46}$$

Eqs. (45)-(46) can be further simplified by noting that from the buoyancy equation (vector form of Eq. (6)),

$$\boldsymbol{V} \cdot \nabla b = -\nabla \cdot (-\kappa \nabla b). \tag{47}$$

Multiplying by $\mathcal{C}$, integrating over the domain and using the chain rule and boundary conditions,

$$\langle \mathcal{C}\boldsymbol{V}\cdot\nabla b\rangle = -\langle \kappa\nabla\mathcal{C}\cdot\nabla b\rangle. \tag{48}$$

Thus the effects of advection and diffusion on the center-of-mass are identical such that Eq. (45) can be written,

$$\frac{\partial\langle b\mathcal{C}\rangle}{\partial t} = -2\langle \kappa\nabla\mathcal{C}\cdot\nabla b\rangle. \tag{49}$$

This surprising result, that advection and diffusion both drive tracer on average in the same direction (despite their influence on buoyancy being exactly opposite), comes about because the tracer is localized. This localization implies that the tracer gradient $\nabla\mathcal{C}$ must change sign, weighting the diapycnal diffusive flux such that tracer is diffused diapycnally on average in the same direction as it is advected diapycnally.

Similarly, multiplying Eq. (47) by $\mathcal{C}(b-\mu_b)$ and integrating over the domain yields,

$$\langle (b-\mu_b)\mathcal{C}\boldsymbol{V}\cdot\nabla b\rangle = \langle (b-\mu_b)\mathcal{C}\nabla\cdot(\kappa\nabla b)\rangle, \tag{50}$$

$$= -\langle \kappa\nabla b\cdot\nabla(\mathcal{C}(b-\mu_b))\rangle, \tag{51}$$

$$= -\langle (b-\mu_b)\kappa\nabla b\cdot\nabla\mathcal{C}\rangle - \langle \kappa\mathcal{C}|\nabla b|^2\rangle. \tag{52}$$

Using Eq. (52), Eq. (46) for the bulk diffusivity can be rewritten as,

$$\kappa_{bk} = -\frac{2}{N^4\langle\mathcal{C}\rangle}\langle \kappa\nabla b\cdot\nabla(\mathcal{C}(b-\mu_b))\rangle + \frac{1}{\langle\mathcal{C}\rangle}\langle \kappa\mathcal{C}\frac{|\nabla b|^2}{N^4}\rangle. \tag{53}$$

If the tracer is mostly outside of the BBL where $|\nabla b|^2 \approx N^4$ then the additional second term is the in-situ diffusivity $\langle\kappa\mathcal{C}\rangle/\langle\mathcal{C}\rangle$. Eqs. (42)-(53) hold generally for any tracer when integrated over a region with zero sources or boundary tracer fluxes. Eqs. (49) and (53) also hold even if the buoyancy field is changing in time.

*b. Boundary and diffusivity gradient contributions to center-of-mass motion*

We now split the buoyancy gradient field from boundary layer theory [Eqs. (1) and (2)] into its background $\nabla B = (B_y, B_z) = N^2(\sin\theta, \cos\theta)$ and perturbation $\nabla b' = (0, b'_z)$ [Eq. (16)] components. Then, using the chain rule and the boundary conditions, the center-of-mass tendency [Eq. (45)] can be expressed as,

$$\langle \mathcal{C} \rangle \frac{\partial \mu_b}{\partial t} = B_y \langle V\mathcal{C} \rangle + \kappa_0 B_z \int_{-\infty}^{\infty} \mathcal{C}(y,0,t)dy + B_z \langle \mathcal{C}\kappa_z \rangle - \langle \kappa \mathcal{C}_z b'_z \rangle, \tag{54}$$

exposing the influence of the boundary (second term on the RHS, which will also be referred to as the "boundary effect") and the diffusivity gradient (third term on the RHS) discussed earlier in the one-dimensional context (Eq. (37), except here multiplied by $B_z$). The final term is associated with variations in the buoyancy gradient in the BBL and is negligible in our context (not shown). The first advective term, as discussed above, is equal to the sum of the three other diffusive terms. We can go even further by identifying the advective tracer fluxes in the BBL and SML with the boundary and diffusivity gradient terms respectively.

*c. BBL and SML contributions to center-of-mass motion*

Recall that the approximate analytic solution derived from one-dimensional boundary layer theory is obtained by combining two solutions (see Appendix A); one for the SML where the diffusivity varies (in the limit $(SPr_{u0})^{-1} \to 0$, Eqs. (67) and (68)), and one for the BBL where the diffusivity is constant and equal to $\kappa_0$ [Eq. (70)]. Therefore,

$$\boldsymbol{V}_{BBL} \cdot \nabla b = \kappa_0 \nabla^2 b, \tag{55}$$

where $\boldsymbol{V}_{BBL} = (\partial \Psi^{BBL}/\partial z)\hat{\boldsymbol{y}}$. Multiplying by $\mathcal{C}$ and integrating as for the derivation of Eq. (48),

$$\langle \mathcal{C}\boldsymbol{V}_{BBL} \cdot \nabla b \rangle = -\kappa_0 \langle \nabla \mathcal{C} \cdot \nabla b \rangle = \kappa_0 B_z \int_{-\infty}^{\infty} \mathcal{C}(y,0,t)dy - \kappa_0 \langle \mathcal{C}_z b'_z \rangle. \tag{56}$$

Thus, the influence of diapycnal tracer advection in the BBL on $\mu_b$ is equivalent to the influence of the boundary term plus a minor correction due to the BBL buoyancy perturbation. In turn, this implies that tracer diapycnal advection in the SML is equivalent to the diffusivity gradient term plus an even smaller correction,

$$\langle \mathcal{C} \boldsymbol{V}_{SML} \cdot \nabla b \rangle = B_z \langle \mathcal{C} \kappa_z \rangle - \langle (\kappa - \kappa_0) \mathcal{C}_z b'_z \rangle . \tag{57}$$

Both of these results match intuition: the boundary effect drives the tracer center-of-mass upward in $b$ whenever there is tracer within the BBL (by limiting tracer diffusion toward denser fluid), as does the upslope BBL diapycnal flow. Similarly, the diffusivity gradient drives the tracer center-of-mass toward denser fluid ($\kappa_z$ is negative), as does the downslope SML diapycnal flow.

For a constant diffusivity there is no SML flow or diffusivity gradient, and so the center-of-mass moves toward lighter water due solely to the influence of BBL advection and the boundary effect, which contribute equally (orange dashed line in Fig. 5b, which when multiplied by 2 provides the full center-of-mass evolution $\mu_b$, the solid line). In the bottom-intensified case, both the diffusivity gradient and the downslope SML transport drive the tracer center-of-mass downward initially (dotted blue line in Fig. 5b, which again should be multiplied by 2 to account for influence of the SML transport), but the boundary effect and advection within the BBL quickly dominates driving the tracer toward less dense fluid on average (solid blue line in Fig. 5b).

*d. BBL and SML contributions to the bulk diffusivity*

Following the same procedures as for the center-of-mass, the bulk diffusivity [Eq. (46)] can be split into contributions from a number of different processes,

$$\kappa_{bk} = \frac{\langle \kappa \mathcal{C} \rangle}{\langle \mathcal{C} \rangle} + \frac{1}{N^4 \langle \mathcal{C} \rangle} \Bigg[ B_y \langle (b-\mu_b) V \mathcal{C} \rangle + \kappa_0 B_z \int_{-\infty}^{\infty} \mathcal{C}(y,0,t)(b(y,0)-\mu_b) dy + B_z \langle \mathcal{C}(b-\mu_b)\kappa_z \rangle - \langle (b-\mu_b)\kappa \mathcal{C}_z b'_z \rangle + B_z \langle \mathcal{C}\kappa b'_z \rangle \Bigg]. \tag{58}$$

As for the simple one-dimensional case considered in Section 5, this equation clearly shows that the bulk diffusivity characterizing the overall spreading rate of tracer across isopycnals is not simply equal to the tracer-weighted isotropic diffusivity or in-situ diffusivity (first term on the RHS, compare solid with dashed lines in Fig. 5c). Instead, there are contributions from advection, from the accumulation of tracer on the boundary, from the vertical gradient in the diffusivity and from the BBL buoyancy perturbation (these last two terms in Eq. (58) related to $b'_z$ are negligible, less than $5 \times 10^{-5} \mathrm{m}^2 \mathrm{s}^{-1}$, in all cases considered here). Once again, the advective term can be split into contributions from the BBL and SML, which identify with the diffusive boundary term and the diffusivity gradient term in Eq. (58) respectively[3]. Eq. (58) provides a useful diagnostic for examining the tracer dispersion. However, it should be noted that the terms are not mutually independent as they all affect and depend on the tracer concentration $\mathcal{C}$.

---

[3]Using Eq. (55) in the advective flux term in Eq. (46),

$$\langle (b-\mu_b)\mathcal{C} \boldsymbol{V}_{BBL} \cdot \nabla b \rangle = \kappa_0 \langle (b-\mu_b)\mathcal{C}\nabla^2 b \rangle \tag{59}$$

$$= -\kappa_0 \langle \nabla (\mathcal{C}(b-\mu_b)) \cdot \nabla b \rangle \tag{60}$$

$$= \kappa_0 B_z \int_{-\infty}^{\infty} \mathcal{C}(y,0,t)(b(y,0,t)-\mu_b) dy - \kappa_0 \langle \frac{\partial}{\partial z} (\mathcal{C}(b-\mu_b)) b'_z \rangle, \tag{61}$$

where we have once again used the chain rule and the boundary conditions. The last term is a minor correction dependent on $b'_z$. In turn Eq. (61) implies that the influence of SML advection is equal to the diffusivity gradient effect (plus another minor correction dependent on $b'_z$).

In the case of a constant diffusivity (orange line in Fig. 5c) the main factor influencing the spreading rate of the tracer across isopycnals, apart from the in-situ diffusivity, is the boundary effect (and equivalently BBL advection). While the influence of the boundary on the center-of-mass motion is always to push the center-of-mass toward less dense fluid (the second RHS term in Eq. (54) is always positive), its influence on the tracer dispersion rate $\kappa_{bk}$ (second term inside the square brackets in Eq. (58)) can have either sign due to the $(b-\mu_b)$ weighting factor. In fact, this term can be further manipulated to yield,

$$\frac{\kappa_0 B_z}{N^4\langle\mathcal{C}\rangle}\left(\int_{-\infty}^{\infty}\mathcal{C}(0)b(0)dy-\mu_b\int_{-\infty}^{\infty}\mathcal{C}(0)dy\right)=\frac{\kappa_0 B_z}{N^4\langle\mathcal{C}\rangle}\langle\mathcal{C}(0)\rangle^y\left(\mu_b^0-\mu_b\right), \tag{62}$$

where $\mathcal{C}(0)$ and $b(0)$ are shorthand for the tracer and buoyancy on the boundary $\mathcal{C}(y,0,t)$ and $b(y,0)$, and $\mu_b^0=\langle b(0)\mathcal{C}(0)\rangle^y/\langle\mathcal{C}(0)\rangle^y$ is the centroid buoyancy of the tracer on the boundary. Thus the boundary effect will generally reduce $\kappa_{bk}$ if $\mu_b^0$ is at a denser level than $\mu_b$ (the usual case, compare closed circles and crosses in Fig. 4)[4]. Its magnitude depends on the separation between $\mu_b^0$ and $\mu_b$ and the amount of tracer on the boundary $\langle\mathcal{C}(0)\rangle^y$. Once again, this boundary effect is equivalent to the influence of BBL advection and can also be understood from this perspective; BBL advection will generally reduce the diapycnal spreading rate as it moves more tracer toward the center-of-mass than away from the center-of-mass (e.g. see Fig. 4a,d).

The reduction in the bulk diffusivity $\kappa_{bk}$ below the in-situ diffusivity (compare dashed and solid lines in Fig. 5c) due to the boundary effect occurs as soon as the tracer encounters the boundary. The behavior of the constant and bottom-intensified diffusivity cases are similar, apart from the magnitude of the initial, and in-situ, diffusivities (compare blue and orange lines in Fig. 5c). This is because the influence of SML advection and the diffusivity gradient are weak (dotted blue line in Fig. 5c). These terms act to drive a modest enhancement of the diapycnal spreading rate as

[4]Of course bizarre tracer distributions where the tracer is in contact with the boundary only above the tracer center-of-mass $\mu_b$ are possible, if unlikely, in which case the boundary effect would enhance $\kappa_{bk}$.

the diapycnal SML velocity is *divergent* around the tracer patch due to the positive curvature in $\kappa$ (since $N^2$ is constant). It is the curvature of $\kappa$ that matters, despite the appearance of only the first-derivative of $\kappa$ in Eq. (58), because of the weighting factor $(b-\mu_b)$.

### *e. Summary*

To summarize, the main effect highlighted by these near-boundary point-release tracer experiments is a strong reduction in the diapycnal spreading rate, below that which would be expected from in-situ measurements of the isotropic diffusivity averaged over the tracer patch[5], due to the presence of the boundary which limits tracer diffusion toward denser water. Accompanying this reduced spreading rate is a tendency for the overall tracer patch, quantified by its center-of-mass, to move up the slope toward less dense fluid. We also showed that due to the buoyancy budget constraint the advective and diffusive fluxes have equivalent influences on the tracer dispersion [Eqs. (49) and (53)], as do their individual BBL and SML contributions. We will discuss these results in the context of field TREs in Section 8. However, in the next section we first examine the sensitivity of the tracer dispersion to several other parameters.

## 7. Sensitivity to other parameters

### *a. Release Location*

In the previous two sections we showed that the presence of the boundary significantly reduces the diapycnal spreading rate of the tracer, and alters the tracer center-of-mass motion. The time-scale over which these effects appear depends on where the tracer is released. When released further from the boundary (e.g. at $z_0 = 3d/4$, Fig. 6a-c) the tracer initially spreads according

[5]Note that this conclusion is not altered if alternative methods of estimating the in-situ diffusivity are considered. For example, the *tracer-gradient* weighted diffusivity $\langle \kappa |C_z| \rangle / \langle |C_z| \rangle$ gives a similar estimate (not shown) consistent with Mashayek et al. (2017).

to the isotropic diffusivity, with enhanced downward diffusion due to bottom-intensification and the downslope SML flow (orange solid line in Fig. 7b). There is an initial slight increase in the bulk diffusivity (solid orange line in Fig. 7c before day $\sim 250$), due to the fact that the SML flow is divergent (dotted orange line in Fig. 7c, which represents the equivalent influence of the diffusivity gradient). However, once the tracer encounters the boundary the diapycnal spreading rate is significantly reduced.

The reduction in the diapycnal spreading rate occurs earlier for tracers released closer to the boundary (e.g. at $z_0 = 62.5$m, Figs. 6d-f and blue lines in Fig. 7). While tracers released very close to the boundary visually appear to experience more overall dispersion (compare Figs. 6f and 6c), most of this dispersion manifests in the lateral direction (despite the absence of any along-isopycnal diffusion) with less spreading across buoyancy surfaces (compare solid blue and orange lines in Fig. 7c). Furthermore, when released close to the boundary the tracer experiences a large upward movement of both its center-of-mass (blue line in Fig. 7b) and overall distribution, such that most of the tracer lies at buoyancies well above its initial buoyancy after 320 days (blue lines in Fig. 7a). This net movement toward less dense fluid is a consequence of the upslope BBL flow and the asymmetric distribution of tracer between the BBL and SML. The latter asymmetry is due to the boundary, which tends to trap tracer in the BBL. The net upward movement of tracer is strongest when the tracer is released next to the boundary, while tracers released away from the boundary in the SML experience a net downward movement (Fig. 8). Field TREs conducted very close to a sloping boundary may be expected to show a similar net diapycnal upward movement of tracer (e.g. Inall 2009). However, in Section 7e we show that the introduction of along-isopycnal diffusion can limit this upward movement.

*b. Topographic Slope*

Though the position of the initial release point of the tracer clearly impacts the initial behavior of the tracer, the slope of the boundary does not in these point release experiments. Altering the slope of the boundary has a number of effects on the boundary layer flow. Firstly, it influences the thickness of the BBL $q_0^{-1}$, with steeper slopes having thinner BBLs (a relatively minor effect due to the fourth-power exponent in Eq. (9), also see Callies and Ferrari 2018). Secondly, it alters the strength of the upslope and downslope boundary layer flows (linearly, due to the factor of $\cot\theta$ in Eq. (11), also compare orange and blue solid lines in Fig. 2a and see Dell and Pratt 2015). The change in the upslope and downslope flow strength arises because the local diapycnal advective flux of buoyancy must remain the same (as the diffusion has not changed), but the separation of buoyancy surfaces in the direction parallel to the boundary changes. Comparing tracer releases performed over a slope of $1/100$ versus $1/400$ shows significant visual differences in the rate of tracer dispersal (Fig. 9). However, the rate of tracer spreading across buoyancy surfaces is in fact almost identical (not shown), because the magnitude of the diapycnal velocity does not change, being set by diffusion. Instead, the spacing of buoyancy surfaces in the $y$ direction ($B_y = N^2 \sin\theta$) increases in proportion to the decrease in upslope flow ($V \sim \cot\theta$), such that the total advective flux of tracer $\langle \mathcal{C}\boldsymbol{V}\cdot\nabla b\rangle = B_y\langle V\mathcal{C}\rangle$ remains the same. However, this result only holds for cases where the tracer is released at a single point. When the tracer is instead released as a horizontal layer, a case considered in Appendix C, the slope of the boundary does influence the spreading rate as it influences the width of the SML and thus the extent to which the tracer is exposed to strong boundary mixing.

### c. Reduced mixing layer stratification

Throughout most of this article we have taken the limit $SPr_{u0}^{-1} \to 0$, where eddies are assumed to flatten isopycnals in the SML and maintain the stratification there. However, observations from the Brazil Basin suggest that isopycnals are often sloped in the active mixing layer and the stratification is reduced (St. Laurent et al. 2001; Ledwell et al. 2000). Callies (2018) found that the observed Brazil Basin stratification was well fitted by the one-dimensional boundary layer solution for a Prandtl number of 230, yielding $SPr_{u0}^{-1} \approx 2$. This corresponds to a three-fold reduction in the SML stratification[6], with a similar reduction in the upslope transport $\Psi$ (Eq. (71) in Appendix A)[7]. This reduction in upslope transport reduces the upslope spreading of tracer (compare Figs. 9d-f and 9g-i) and the net movement of tracer toward lighter fluid (as the upslope buoyancy gradient $b_y$ remains the same). The rate of increase of the variance of the tracer in buoyancy space also reduces. However, the bulk diffusivity includes a stratification normalization factor [Eq. (23)] which, as the tracer does not extend beyond the SML, in this case should be chosen as the SML stratification $N^2/(1+SPr_{u0}^{-1})$. With this normalization factor the bulk diffusivity and its contributions from the boundary effect, the diffusivity gradient and BBL and SML advection remain almost compared with the $SPr_{u0}^{-1} = 0$ case (not shown). This implies that the slope of the isopycnals (independent of the change in $N^2$) has only a minor impact on the tracer dispersion. However, this may no longer be true for tracer clouds that extend across the entire SML into the far-field.

### d. Decay scale of bottom-intensified mixing

The tracer dispersion is also sensitive to the decay scale used for the isotropic diffusivity [$d$ in Eq. (10)]. When the tracer is released at the same distance from the boundary but this $d$ scale is

[6]Note that all our tracer experiments are conducted within the SML and do not extend into the far-field, defined by the distance $d\log(\kappa_0/\kappa_\infty)$ (Callies 2018) where the stratification does eventually return to $N^2$.

[7]There is also a small factor of $3^{1/4}$ modification to the BBL scale $q_0$ (Eq. (9)).

reduced to 200m (a value that may be more representative of the Brazil Basin, St. Laurent et al. 2001; Callies 2018) then the tracer remains restricted closer to the boundary and the net upslope movement of the tracer toward lighter buoyancy is reduced (compare Figs. 9j-l with 9a-c). The reduction in the center-of-mass movement in buoyancy space is due to the increase in the vertical gradient of the isotropic diffusivity $\kappa_z$, or equivalently an increase in the SML transport, that drives more tracer downward (compare blue and orange dotted and dashed lines in Fig. 10b). This increase in the vertical gradient of the diffusivity also acts to enhance the tracer spreading rate in buoyancy space such that the bulk diffusivity does not reduce as much as would be expected from the reduced in-situ diffusivity (compare orange and blue lines in Fig. 10c).

*e. Influence of along-isopycnal diffusion*

Finally we consider the impact of along-isopycnal diffusion on the tracer behavior. Large along-isopycnal diffusion may be expected in abyssal mixing layers due to processes such as intrusions (e.g. McPhee-Shaw 2006) or baroclinic instability setup by boundary mixing (e.g. Callies 2018; Wenegrat et al. 2018). Along-isopycnal diffusion can rapidly mix tracer between the SML and BBL, an effect which is clear when comparing TREs with large ($A_H = 100\text{m}^2\text{s}^{-1}$, Fig. 11d-f) and small ($A_H = 10\text{m}^2\text{s}^{-1}$, Fig. 11a-c) along-isopycnal diffusivities. The along-isopycnal diffusivity also appears to influence the spreading of the tracer in buoyancy space, despite the inability of along-isopycnal diffusion to directly flux tracer across isopycnals (Fig. 12). At early times, the enhanced along-isopycnal diffusion limits the initial downward motion of the center-of-mass by mixing tracer more rapidly into the BBL, enhancing the boundary effect (compare orange and blue solid and dashed lines in Fig. 12b before day 500). However, at later times along-isopycnal diffusion limits the motion of the center-of-mass up the slope toward less dense fluid as the tracer is mixed between the regions of upslope and downslope motion in the BBL and SML respectively.

In terms of the framework introduced in Section 6, the limited upslope motion of the center-of-mass arises because of a reduction in the influence of BBL advection (or equivalently the boundary effect, compare dashed lines in Fig. 12b after day 1000), as there is less tracer in contact with the boundary.

Similarly, the reduction of the influence of the boundary, or BBL advection, on the tracer distribution under strong along-isopycnal diffusion results in an enhanced rate of diapycnal spreading as quantified by $\kappa_{bk}$ (compare solid blue and orange lines in Fig. 12c). The magnitude of the boundary effect responsible for the reduction in $\kappa_{bk}$ is dependent on two factors [Eq. (62)]; 1) the amount of tracer on the boundary $\langle \mathcal{C}(0) \rangle^y$ and 2) the buoyancy spacing between the total tracer center-of-mass $\mu_b$ and that on the boundary $\mu_b^0$. Large along-isopycnal diffusion decreases both of these factors by moving tracer away from the boundary on average and by homogenizing the tracer between the boundary and SML such that $\mu_b^0 - \mu_b$ is reduced (compare positions of closed circles and crosses in Fig. 11). The second of these two factors generally dominates (not shown).

A secondary effect of along-isopycnal diffusion is to reduce the in-situ diffusivity averaged over the tracer patch (compare dashed blue and orange lines in Fig. 12c) by driving a net lateral movement of tracer toward the weakly mixing interior. This net lateral movement toward the far-field with along-isopycnal diffusion is once again due to the presence of the boundary that prevents tracer transport through it.

The results of these experiments are summarized in Fig. 13, where three measures of the time-averaged or cumulative diffusivity up to day 800 are shown for a range of along-isopycnal diffusivities[8]. For all values of $A_H$ the total diapycnal spreading rate of tracer across-isopycnals, as quantified by the bulk diffusivity, is smaller than the in-situ diffusivity (compare circles and crosses

[8]We do not include a similar summary figure for the dependence of the center-of-mass motion on $A_H$ as this depends strongly on the time-scale of interest (compare blue and orange solid lines in Fig. 12b).

in Fig. 13). As along-isopycnal diffusion increases the diapycnal spreading rate increases and the in-situ diffusivity decreases. The enhancement of diapycnal tracer fluxes by along-isopycnal diffusion (which has no influence on buoyancy) is a salient result which stems from the presence of the boundary and interactions between the tracer gradients and diapycnal diffusion. Finally, a more sophisticated estimate of the tracer derived diffusivity discussed in Appendix B, based on a least-squares fit to the results of a one-dimensional advection-diffusion equation, gives similar results to the bulk diffusivity (compare triangles and circles in Fig. 13), meaning that if this estimate was interpreted as a measure of the in-situ diffusivity it would be an under-estimate.

## 8. Relation to field experiments

Our study has focused on tracer behavior in the immediate boundary region, as opposed to past field TREs such as BBTRE and DIMES. Nevertheless, it is useful to discuss our results in the context of these past experiments. The BBTRE tracer (Ledwell et al. 2000) was released along a target isopycnal that sat about 1000m above the bottom of a fracture zone trough. Much of the tracer cloud thus lay in the outer SML, although because of topographic variability some tracer was located much closer to the boundary (Fig. 4 of Ledwell et al. 2000). The initial tracer dispersion was well modeled with a one-dimensional advection-diffusion equation and showed a tendency to move downward toward denser water (Fig. 2a of Ledwell et al. 2000), consistent with our results for bottom-intensified mixing (e.g. Fig. 6a-c). A smaller portion of the tracer was also drawn eastward and more strongly downward toward the MAR boundary. Once significant amounts of tracer came into contact with the boundary Ledwell et al. (2000) point out that the tracer tended to get mixed back toward lighter density levels, consistent with the boundary effect presented in this paper. During this later time period Ledwell et al. (2000) do not attempt to use a one-dimensional model for these later periods of BBTRE, as it would likely underestimate the

diffusivity. We have applied such a one-dimensional model to our idealized experiments and found that it provides a similar estimate of the diapycnal tracer spreading rate to the bulk diffusivity $\kappa_{bk}$ (see Appendix B), and therefore indeed underestimates the in-situ diffusivity $\langle \kappa \mathcal{C} \rangle / \langle \mathcal{C} \rangle$. In our case this underestimate is roughly a factor of 3 (Fig. A3). However, in the BBTRE case (all else being equal) we would expect a more accurate result as a larger proportion of the tracer lies in the interior where the boundary has less impact. In Appendix C we examine tracers released as a strip extending further into the interior where we indeed find that the boundary has less influence. However, we also find that a one-dimensional model has some difficulty modeling this case due to the spatial variation in the isotropic diffusivity across the tracer patch.

Our results have less immediate applicability to DIMES, given the topographic complexity and strong mean flows characterizing the Southern Ocean. In particular, we note that the order-of-magnitude mismatch between diffusivities estimated from the DIMES tracer and microstructure observations cannot be explained using the physics discussed here. The boundary effect discussed in this study would suggest that in-situ estimates should exceed those obtained from the tracer measurements rather than the other way around, and by less than an order-of-magnitude.

While neither BBTRE or DIMES were specifically designed to study near boundary tracer dispersion, future experiments are planned with this aim. The relations derived in this article may help in the analysis of these experiments. Firstly, the realization that there is some equivalence between the effects of diapycnal advection and diffusion on the tracer moments in buoyancy space [e.g. Eqs. (49) and (53), which hold generally providing boundary tracer fluxes and interior sources can be eliminated] may allow some calculations to be simplified. For example, if the change in the center-of-mass density of the tracer patch $\Delta \langle bC \rangle$ over a specified time period is measured, then by

time-integrating Eq. (49), using the chain rule and eliminating the boundary term,

$$\overline{\langle \mathcal{C}\, \nabla \cdot (\kappa \nabla b) \rangle} = \frac{\Delta \langle bC \rangle}{2}, \tag{63}$$

where the over line indicates a time-integral. Eq. (63) allows the convergence of the diffusive buoyancy flux, or net buoyancy source $Db/Dt$, averaged over the tracer patch to be easily obtained.

Secondly, if detailed information is available (perhaps as part of a series of surveys of the initial spreading of tracer) then it may be possible to utilize some of our relations to better infer properties of the underlying turbulent diffusivity. For example, if a structure $f(\tilde{z})$ of the turbulent diffusivity as a function of distance above bottom $\tilde{z}$ was assumed (such that $\kappa(\tilde{z}) = \kappa_0 f(\tilde{z})$ with $f(0) = 1$), then substitution into Eq. (58) and some rearrangement (where we have also, for the point of argument, ignored the terms dependent on $b_z'$, and removed the advective term in favor of multiplying the diffusive terms by 2 as shown in Eq. (53)) yields,

$$\kappa_0 \approx \langle \mathcal{C} \rangle \kappa_{bk} \left\{ \langle f\mathcal{C} \rangle + 2N^{-2} \cos\theta \left[ \langle \mathcal{C}(0)\,(b(0) - \mu_b) \rangle^y + \langle \mathcal{C}(b - \mu_b) f_z \rangle \right] \right\}^{-1}. \tag{64}$$

If the three-dimensional tracer moments $\langle b\mathcal{C} \rangle$, $\langle b^2\mathcal{C} \rangle$, $\kappa_{bk}$, along with the shape function correlations $\langle f\mathcal{C} \rangle$, $\langle \mathcal{C}(b - \mu_b) f_z \rangle$ and the concentrations of tracer near the boundary $\langle \mathcal{C}(0) \rangle^y$ and $\langle \mathcal{C}(0) b(0) \rangle^y$ can be measured, then Eq. (64) provides an estimate of the peak near-bottom diffusivity $\kappa_0$ taking into account the boundary and $\kappa_z$ effects. Nevertheless, it remains unclear whether these time- and space-averaged tracer correlations can be estimated with sufficient accuracy given sampling limitations in the field.

Finally, it may also be possible to use the knowledge and relations gained from this study to build an intermediate complexity prognostic model of the tracer dispersion that is simplified relative to the full 2D or 3D problem but takes into account some of the boundary effects neglected by the 1D advection-diffusion model considered in Appendix B. A more comprehensive inverse model along these lines may allow better estimates of the properties of the small-scale turbulent diffusivity to

be obtained from the sparsely sampled tracer data. The development of such a model is, however, outside the scope of this article.

## 9. Summary

We have examined the behavior of a passive tracer released near a sloping boundary within a flow governed by one-dimensional boundary layer theory. Results can be summarized as follows:

1. For isolated near-boundary tracer releases the presence of the *boundary reduces the net diapycnal tracer spreading rate* below that which would be expected from averaging the in-situ diffusivity over the tracer patch (Figs. 5c and 13).

2. The dipole of diapycnal flow, upward in the BBL and downward in the SML, also influences the tracer dispersion. In particular, when the tracer is released close to the boundary it tends to move *upslope toward less dense fluid on average* (e.g. Fig. 4d-f) due to the asymmetric distribution of diapycnal flow between the BBL and SML (the SML flow being spread over a much wider region). However, the extent of this upslope motion depends on the proximity of the tracer release point to the boundary (Fig. 6) with tracers released further from the boundary in the outer SML experiencing a downward net diapycnal motion (as summarized by Fig. 8).

3. As a consequence of the advection-diffusion balance in the buoyancy equation, there is an *equivalence between the diffusive and advective tracer fluxes*; they both contribute equally to the domain-averaged diapycnal tracer flux [Eq. (48)]. Further, the slowing of the diapycnal tracer spreading rate due to the presence of the boundary is equivalent to the influence of tracer advection within the BBL, while the modest enhancement in tracer spreading associated with

the divergent diapycnal flow in the SML is equivalent to the diffusive influence of the gradient in the isotropic diffusivity.

4. For point release experiments the boundary slope has little effect on the diapycnal spreading rate.

5. The introduction of reduced stratification and sloping isopycnals in the SML (Callies 2018) reduces the rate at which tracer spreads across isopycnals. However, as a diffusivity measures the rate of tracer spreading in physical space the bulk diffusivity does not change.

6. When the decay scale of bottom-intensified mixing is decreased then the overall tracer spreading across isopycnals decreases. However, this decrease is not as much as would be expected from the change in in-situ diffusivity because the SML transport becomes more divergent.

7. *Along-isopycnal diffusion enhances the diapycnal tracer spreading rate* for near-boundary point releases by reducing the damping influence of the boundary and BBL advection (Fig. 13). Along-isopycnal diffusion also drives more tracer away from the boundary to where mixing is weak, reducing the in-situ diffusivity averaged over the tracer patch.

While the differences in diffusivity arising from the additional boundary effects exposed in this study are generally less than an order of magnitude, our results nevertheless highlight the complexity of tracer behavior near sloping boundaries. Additional complexities present in the observational context likely make matters worse. Variations in topographic slope, mixing intensity and stratification are likely to drive additional tracer transports. Submeso- to large-scale currents will also drive interactions between the tracer patch and different boundaries at a range of depths, buoyancies and times. It is possible that averaging over these complexities will result in smooth Gaussian tracer spreading across buoyancy surfaces with a well-defined central diffusivity. However, our results suggest that relating this tracer-derived diffusivity to the small-scale turbulent diffusivity

important for buoyancy and mass transport must be done with care. In Section 8 we discussed several avenues that may help with the analysis of future near-boundary TREs.

Further modeling work is also needed to assess the impact of additional complexities. For example, a large *net* up- or down-slope mass transport associated with upslope variations in topography, stratification or mixing may influence the tracer behavior. The role of intrusions of boundary layer fluid into the interior (e.g., Gloor et al. 2000) is another area that deserves further attention. In this article, the influence of such intrusions on tracer transport was captured at first-order through an along-isopycnal diffusivity. Such an approximation may be appropriate for the statistical average tracer behavior, but is less applicable to a tracer released, for example, at a particular phase of a passing eddy. Finally, the relationship between the along-isopycnal diffusion and the eddy-driven overturning required to maintain a stratified SML in rotating boundary layer theory (e.g. Callies 2018), and whether this influences the tracer transport, is worthy of further exploration. A deep understanding of these processes is needed in order to represent them appropriately in general circulation models.

*Acknowledgments.* We gratefully acknowledge support from the Australian Research Council through grant FL150100090. We thank Geoff Vasil for help with the Dedalus simulations. We thank Jörn Callies and an anonymous reviewer for useful comments. This research was undertaken with the assistance of resources and services from the National Computational Infrastructure (NCI), which is supported by the Australian Government.

## Appendix A: The approximate analytic solution

Here we present the derivation of the approximate analytic solution to one-dimensional boundary layer theory with a bottom-intensified diffusivity [Eq. (10)] following Callies (2018) (note that our derivation differs from Callies (2018) through the use of distinct viscosities in the $x$ and $y$

directions). We non-dimensionalize the boundary layer equations using,

$$\kappa = \kappa_0 \hat{\kappa}, \quad \nu_u = \nu_{u0} \hat{\kappa}, \quad \nu_v = \nu_{v0} \hat{\kappa}, \quad z = d\,\hat{z}, \quad \Psi = \kappa_0 \cot\theta \hat{\Psi}, \tag{65}$$

where $\kappa_0$, $\nu_{u0}$ and $\nu_{v0}$ represent the near-boundary diffusivity and viscosity. Eq. (7) then becomes,

$$\frac{d^2}{d\hat{z}^2}\left(\hat{\kappa}\frac{d^2\hat{\Psi}}{d\hat{z}^2}\right) + 4(dq_0)^4\left(\frac{\hat{\Psi}}{\hat{\kappa}} - \frac{1+(SPr_{u0})^{-1}\frac{r}{\hat{\kappa}}}{1+(SPr_{u0})^{-1}}\right) = 0, \tag{66}$$

where $r = \kappa_\infty/\kappa_0$, $q_0$ is the BBL width parameter based on the mixing coefficients near the boundary [Eq. (9)] and we have assumed constant Prandtl numbers $Pr_{u0}$ and $Pr_{v0}$. For reasonable deep ocean parameters $q_0^{-1} \sim 4.5$m (or $q_0^{-1} = 28$m for small $(SPr_{u0})^{-1}$ where $q_0$ is determined by upslope friction only, see Eq. (9)). Therefore, with $d \sim 500$m, $dq_0 \sim 20$ the fourth derivative term in Eq. (66) can be ignored outside the thin BBL. Following Garrett (2001), a solution outside the BBL is therefore (restoring the dimensions),

$$\Psi^{SML} = \frac{\cot\theta}{1+(SPr_{u0})^{-1}}\left(\kappa + (SPr_{u0})^{-1}\kappa_\infty\right) \tag{67}$$

$$\frac{\partial b}{\partial z}^{SML} = N^2\frac{\cos\theta}{1+(SPr_{u0})^{-1}}\left(1+(SPr_{u0})^{-1}\frac{\kappa_\infty}{\kappa}\right) \tag{68}$$

For large $(SPr_{u0})^{-1}$, this gives much reduced stratification over the entire SML until $\kappa$ approaches $\kappa_\infty$ (Callies 2018).

Eqs. (67) and (68) provide a solution in the SML, but do not satisfy the boundary conditions $\Psi = 0$ and $\partial\Psi/\partial z = 0$ at $z = 0$. To satisfy these boundary conditions we introduce an inner BBL solution where the fourth derivative term in Eq. (66) becomes important. For this inner solution we can make the assumption that the mixing coefficients are constant $\kappa \sim \kappa_0$, $\nu_u \sim \nu_{u0}$, $\nu_v \sim \nu_{v0}$. With $\Psi = \Psi^{BBL} + \Psi^{SML}$, where $\Psi^{SML}$ is assumed constant in the BBL, substitution into Eq. (7) yields,

$$\frac{d^4\Psi^{BBL}}{dz^4} + 4q_0^4\Psi^{BBL} = 0, \tag{69}$$

The solution that satisfies the boundary condition $\Psi^{BBL}(0) = -\Psi^{SML}(0)$ and $\partial\Psi^{BBL}/\partial z(0) = 0$ (neglecting the small $\partial\Psi^{SML}/\partial z$ at $z = 0$) is given by,

$$\Psi^{BBL} = -\frac{\cot\theta}{1+(SPr_{u0})^{-1}}\left(\kappa_0 + (SPr_{u0})^{-1}\kappa_\infty\right)e^{-q_0 z}\left(\cos q_0 z + \sin q_0 z\right), \tag{70}$$

so that the full approximate solution is,

$$\Psi = \frac{\cot\theta}{1+(SPr_{u0})^{-1}}\left(\kappa + (SPr_{u0})^{-1}\kappa_\infty\right)\left(1 - e^{-q_0 z}\left(\cos q_0 z + \sin q_0 z\right)\right), \tag{71}$$

where we have also used the fact that $\kappa_0 e^{-q_0 z}(\cos q_0 z + \sin q_0 z) \approx \kappa e^{-q_0 z}(\cos q_0 z + \sin q_0 z)$. In the limit $(SPr_{u0})^{-1} \to 0$ Eq. (71) reduces to Eq. (11), which will be used to determine the upslope velocity $V = \partial\Psi/\partial z$ and buoyancy field $b_z = N^2 \sin\theta\, \Psi/\kappa$ for the 2D tracer release experiments.

## Appendix B: A one-dimensional model of the tracer dispersion across isopycnals

In this appendix we apply a one-dimensional model, commonly used in field TREs (e.g. Ledwell and Watson 1991; Ledwell 1998) to the evolution of the tracer distribution in buoyancy space. The tracer evolution is modeled using the one-dimensional equation,

$$\frac{\partial\overline{\mathcal{C}}}{\partial t} + (\overline{w} - \overline{\kappa}_h)\frac{\partial\overline{\mathcal{C}}}{\partial h} = \overline{\kappa}\frac{\partial^2\overline{\mathcal{C}}}{\partial h^2}, \tag{72}$$

where the over line denotes an area-average on isopycnals at a given height $h$ above a target buoyancy surface. A mean stratification profile is used to convert between $h$ and $b$. The area-averaged diffusivity is assumed to be a linear function of $h$, $\overline{\kappa} = \overline{\kappa}_0 + h\overline{\kappa}_h$. Following Ledwell and Watson (1991) and Ledwell (1998), we discretize Eq. (72) using a forward-in-time, centered-in-space discretization and minimize the sum of squares,

$$\sum_h \left(\mathcal{C}_n^{obs} - L^n\mathcal{C}_0\right), \tag{73}$$

with respect to the three parameters $\overline{\kappa}_0$, $\overline{w}$ and $\overline{\kappa}_h$. The sum is performed over the discretized height $h$. Here $\mathcal{C}_n^{obs}$ is the distribution of tracer in buoyancy space from the full 2D simulation at

a given time $t_n$, $L$ is a matrix operator representing the centered-in-space spatial discretization of Eq. (72) and $\mathcal{C}_0$ is the initial tracer distribution[9].

The model matches the evolution of the buoyancy tracer profiles from the full two-dimensional simulations very well for both constant (not shown) and bottom-intensified (compare solid lines and open circles in Fig. A1a) diffusivity cases. The least-squares fit provides an estimate of a single diffusivity and its linear gradient over the full evolution of the tracer up to a given time. This diffusivity, at the center-of-mass position of the fitted tracer distribution, compares well with the time-averaged bulk diffusivity measured from the tracer moments (compare solid blue and orange lines in Fig. A1b). In particular, the fitting method reproduces the rapid initial decrease in the tracer spreading rate below that expected from the in-situ diffusivity due to the presence of the boundary[10].

The least-squares fit also provides estimates of a mean diapycnal velocity $\overline{w}$ and diffusivity gradient (solid and dashed lines in Fig. A1c respectively). The fit predicts negative values for $\overline{w}$ and $\overline{\kappa_h}$ at initial times before the tracer contacts the boundary, consistent with what would be expected within the SML. However, at later times $\overline{\kappa}_h$ is predicted as positive. Integrating Eq. (72) over all $h$ shows that the rate of change of the center-of-mass $\mu_h$ and the one-dimensional bulk diffusivity in the one-dimensional model are given by,

$$\frac{\partial \mu_h}{\partial t} = \overline{w} + \overline{\kappa}_h \tag{74}$$

$$\kappa_{bk}^{1D} = \frac{1}{2}\frac{\partial \sigma_h^2}{\partial t} = \frac{\langle \overline{\kappa}\mathcal{C}\rangle^h}{\langle \mathcal{C}\rangle} = \overline{\kappa}_h \mu_h + \overline{\kappa}_0 \tag{75}$$

[9] We use a non-linear Levenberg-Marquardt least-squares minimization algorithm (Moré 1978). The spatial discretization uses a regular height grid with 100-points converted from buoyancy space using the far-field stratification $N^2$. The time step is 1 day.

[10] However, if the presence of a boundary *at a particular value of b* was known, then this could be included in the boundary conditions of the one-dimensional model and a better estimate of the in-situ diffusivity could be obtained. In a field TRE boundaries are likely present at varying depths and buoyancies over the history of the experiment, and thus this knowledge is unlikely.

Thus, the positive $\overline{w}$ and $\overline{\kappa}_h$ at later times are present in order to drive the center-of-mass toward less dense fluid [Eq. (74)]. In the full two-dimensional case this center-of-mass movement is achieved by the boundary effect and BBL advection, that are not captured by the one-dimensional model [they do not appear in Eq. (74)]. Further, in the one-dimensional model the bulk diffusivity is equal to the one-dimensional in-situ diffusivity $\langle\overline{\kappa}\mathcal{C}\rangle^h/\langle\mathcal{C}\rangle$, which in turn is equal to the diffusivity at the tracer center-of-mass position $\mu_h$ [Eq. (75)]. Comparing Eq. (75) to Eq. (58), the boundary effect, the advective term and the diffusivity gradient term in Eq. (58) all drop out because $\overline{w}$ and $\kappa_h$ are constants and can be removed from the averaging leaving the factor $\langle(h-\mu_h)\mathcal{C}\rangle = 0$. Thus, the one-dimensional model, while reproducing the evolution of the tracer variance in buoyancy space, assigns all of that spreading rate to the *in-situ* diffusivity $\overline{\kappa}$. Because we found the spreading rate to be less than expected from the in-situ diffusivity, the 1D method would thus yield a much reduced in-situ diffusivity compared to that actually acting on the tracer $\langle\kappa\mathcal{C}\rangle/\langle\mathcal{C}\rangle$.

## Appendix C: Tracer released as a layer

We have investigated the spreading of a tracer released at a single location near the boundary, within the actively mixing layer. Different behavior may be expected in the case where a tracer is released outside the mixing layer, is homogenized along-isopycnals, and only later interacts with the boundary. In this appendix we examine an idealized example of such a case where the tracer is released as a layer spread horizontally and centered around a particular buoyancy surface (see Fig. A2: the tracer is released within the dashed white box). To emphasize the boundary effects we release the tracer as a strip extending only across the SML.

Enhanced vertical diffusion of the tracer patch occurs in the region close to the boundary (Fig. A2c). The near-boundary tracer spreads further up than down the slope as a consequence of the

BBL flow as for the point-release experiments (e.g. Fig. 4). However, the center-of-mass motion is much weaker here, because the majority of the tracer patch experiences only weak diffusion (solid lines in Fig. A3b).

When a larger proportion of tracer is located further from the boundary the bulk diffusivity is more comparable to the in-situ diffusivity (compare dashed and solid lines in Fig. A3c, and compare to the point-release cases in Fig. 5). This is because the damping effect of the boundary depends on the ratio of tracer near the boundary versus away from the boundary, $\langle \mathcal{C}(0) \rangle^y / \langle \mathcal{C} \rangle$ [see Eq. (62)]. As the initial tracer patch is extended further into the far-field the in-situ and bulk diffusivities weaken and converge (compare orange and blue lines in Fig. A3c). The addition of along-isopycnal diffusion also drives more tracer into the far-field where mixing is weak, acting to reduce both the in-situ and bulk diffusivities (Fig. A4). This contrasts with the near-boundary point-release experiments where along-isopycnal diffusion enhanced the diapycnal spreading rate by reducing the boundary effect (Fig. 13). In the layer cases the boundary effect is already weak and so the enhancement of tracer movement away from the boundary dominates.

Finally, when the tracer is released as a layer the tracer profiles in buoyancy space evolve in a manner which is not as well captured by the one-dimensional advection-diffusion equation considered in Appendix B (compare solid and dotted lines in Fig. A3a), compared to the point-release cases (e.g. Fig. A1a). The tracer buoyancy profiles in the layer case exhibit more rapid spreading of the tails of the distribution and slower spreading of the core of the distribution (associated with the near-boundary and weak-diffusion far-field regions respectively, Fig. A2). The 1D advection-diffusion equation with constant parameters $\overline{w}$, $\overline{\kappa}_h$ and $\kappa_0$ [e.g. Eq. (72)] cannot capture this behavior, as the constant velocity and linear diffusivity can drive the development of skewness but not of kurtosis in the distribution. It is possible that a 1D advection-diffusion equation with a diffusivity that was quadratically dependent on $h$, for example, may be able to capture this behav-

ior. However, such a model is not supported by the setting. Due to this difficulty the diffusivity predicted by the one-dimensional method does not provide as good an estimate of the overall spreading rate of the tracer, predicting a weaker value (compare triangles to open circles in Fig. A4). It is possible that a similar problem may manifest in field experiments when a tracer encounters a boundary where mixing is enhanced, or in any situation where the tracer patch spreads over two regions with very different mixing characteristics. Providing that the tracer is sampled in both regions, then this effect can be identified from the non-standard behavior of the tracer distributions in buoyancy space. However, if the near-boundary regions where diffusion is strong are not sampled then the diffusivity may be underestimated.

## References


Armi, L., 1978: Some evidence for boundary mixing in the deep ocean. *J. Geophys. Res.*, **83 (C4)**, 1971–1979, doi:10.1029/JC083iC04p01971.

Banyte, D., D. A. Smeed, and M. M. Morales, 2018: The weakly stratified bottom boundary layer of the global ocean. *J. Geophys. Res.*, **123**, 5587–5598, doi:10.1029/2018JC013754.

Burns, K. J., G. M. Vasil, J. S. Oishi, D. Lecoanet, and B. P. Brown, 2019: Dedalus: A Flexible Framework for Numerical Simulations with Spectral Methods. *arXiv.org*, arXiv:1905.10388, May 2019.

Callies, J., 2018: Restratification of abyssal mixing layers by submesoscale baroclinic eddies. *J. Phys. Oceanogr.*, **48 (9)**, 1995–2010, doi:10.1175/JPO-D-18-0082.1.

Callies, J., and R. Ferrari, 2018: Dynamics of an abyssal circulation driven by bottom-intensified mixing on slopes. *J. Phys. Oceanogr.*, **48 (6)**, 1257–1282, doi:10.1175/JPO-D-17-0125.1.

915 Csanady, G. T., 1969: Diffusion in an Ekman layer. *J. Atmos. Sci.*, **26 (3)**, 414–426, doi:10.1175/
916 1520-0469(1969)026⟨0414:DIAEL⟩2.0.CO;2.

917 de Lavergne, C., G. Madec, J. Le Sommer, A. J. G. Nurser, and A. C. Naveira Garabato, 2016: On
918 the consumption of Antarctic Bottom Water in the abyssal ocean. *J. Phys. Oceanogr.*, **46 (2)**,
919 635–661, doi:10.1175/JPO-D-14-0201.1.

920 de Lavergne, C., G. Madec, F. Roquet, R. M. Holmes, and T. J. McDougall, 2017: Abyssal
921 ocean overturning shaped by seafloor distribution. *Nature*, **551 (7679)**, 181–186, doi:10.1038/
922 nature24472.

923 Dell, R. W., and L. J. Pratt, 2015: Diffusive boundary layers over varying topography. *J. Fluid*
924 *Mech.*, **769**, 635–653, doi:10.1017/jfm.2015.88.

925 Ferrari, R., A. Mashayek, T. J. McDougall, M. Nikurashin, and J.-M. Campin, 2016: Turn-
926 ing ocean mixing upside down. *J. Phys. Oceanogr.*, **46 (7)**, 2239–2261, doi:10.1175/
927 JPO-D-15-0244.1.

928 Garrett, C., 1990: The role of secondary circulation in boundary mixing. *J. Geophys. Res.*, **95 (C3)**,
929 3181–3188, doi:10.1029/JC095iC03p03181.

930 Garrett, C., 1991: Marginal mixing theories. *Atmosphere-Ocean*, **29 (2)**, 313–339, doi:10.1080/
931 07055900.1991.9649407.

932 Garrett, C., 2001: An isopycnal view of near-boundary mixing and associated flows. *J. Phys.*
933 *Oceanogr.*, **31 (1)**, 138–142, doi:10.1175/1520-0485(2001)031⟨0138:AIVONB⟩2.0.CO;2.

934 Garrett, C., P. MacCready, and P. Rhines, 1993: Boundary mixing and arrested Ekman layers:
935 Rotating stratified flow near a sloping boundary. *Annu. Rev. Fluid Mech.*, **25 (1)**, 291–323.

936 Gent, P. R., and J. C. McWilliams, 1990: Isopycnal mixing in ocean circulation models. *J. Phys.*
937 *Oceanogr.*, **20 (1)**, 150–155, doi:10.1175/1520-0485(1990)020⟨0150:IMIOCM⟩2.0.CO;2.

938 Gent, P. R., J. Willebrand, T. J. McDougall, and J. C. McWilliams, 1995: Parameterizing eddy-
939 induced tracer transports in ocean circulation models. *J. Phys. Oceanogr.*, **25 (4)**, 463–474,
940 doi:10.1175/1520-0485(1995)025⟨0463:PEITTI⟩2.0.CO;2.

941 Gloor, M., A. Wüest, and D. M. Imboden, 2000: Dynamics of mixed bottom boundary layers
942 and its implications for diapycnal transport in a stratified, natural water basin. *J. Geophys. Res.*,
943 **105 (C4)**, 8629–8646, doi:10.1029/1999JC900303.

944 Goudsmit, G.-H., F. Peeters, M. Gloor, and A. Wüest, 1997: Boundary versus internal diapycnal
945 mixing in stratified natural waters. *J. Geophys. Res.*, **102 (C13)**, 27 903–27 914, doi:10.1029/
946 97JC01861.

947 Greatbatch, R. J., and K. G. Lamb, 1990: On parameterizing vertical mixing of momentum
948 in non-eddy resolving ocean models. *J. Phys. Oceanogr.*, **20 (10)**, 1634–1637, doi:10.1175/
949 1520-0485(1990)020⟨1634:OPVMOM⟩2.0.CO;2.

950 Holmes, R. M., C. de Lavergne, and T. J. McDougall, 2018: Ridges, seamounts, troughs,
951 and bowls: Topographic control of the dianeutral circulation in the abyssal ocean. *J. Phys.*
952 *Oceanogr.*, **48 (4)**, 861–882, doi:10.1175/JPO-D-17-0141.1.

953 Inall, M. E., 2009: Internal wave induced dispersion and mixing on a sloping boundary. *Geophys.*
954 *Res. Lett.*, **36 (5)**, doi:10.1029/2008GL036849, l05604.

955 Ivey, G. N., 1987a: Boundary mixing in a rotating, stratified fluid. *J. Fluid Mech.*, **183**, 2544,
956 doi:10.1017/S0022112087002507.

957 Ivey, G. N., 1987b: The role of boundary mixing in the deep ocean. *J. Geophys. Res.*, **92 (C11)**,
958 11 873–11 878, doi:10.1029/JC092iC11p11873.

959 Kunze, E., 2017a: The internal-wave-driven meridional overturning circulation. *J. Phys.*
960 *Oceanogr.*, **47 (11)**, 2673–2689, doi:10.1175/JPO-D-16-0142.1.

961 Kunze, E., 2017b: Internal wave-driven mixing: Global geography and budgets. *J. Phys.*
962 *Oceanogr.*, **47 (6)**, 1325–1345, doi:10.1175/JPO-D-16-0141.1.

963 Ledwell, J., 1998: Mixing of a tracer in the pycnocline. *J. Geophys. Res.*, **103 (C10)**, 21 499–
964 21 529, doi:10.1029/98JC01738.

965 Ledwell, J. R., and A. Bratkovich, 1995: A tracer study of mixing in the Santa Cruz Basin. *J.*
966 *Geophys. Res.*, **100 (C10)**, 20 681–20 704, doi:10.1029/95JC02164.

967 Ledwell, J. R., L. C. S. Laurent, J. B. Girton, and J. M. Toole, 2011: Diapycnal mixing
968 in the Antarctic Circumpolar Current. *J. Phys. Oceanogr.*, **41 (1)**, 241–246, doi:10.1175/
969 2010JPO4557.1.

970 Ledwell, J. R., E. T. Montgomery, K. L. Polzin, L. C. St. Laurent, R. W. Schmitt, and J. M.
971 Toole, 2000: Evidence for enhanced mixing over rough topography in the abyssal ocean. *Nature*,
972 **403 (6766)**, 179–182, doi:10.1038/35003164.

973 Ledwell, J. R., and A. J. Watson, 1991: The Santa Monica Basin tracer experiment: A study of di-
974 apycnal and isopycnal mixing. *J. Geophys. Res.*, **96 (C5)**, 8695–8718, doi:10.1029/91JC00102.

975 Ledwell, J. R., A. J. Watson, and C. S. Law, 1993: Evidence for slow mixing across the pycnocline
976 from an open-ocean tracer-release experiment. *Nature*, **364**, 701–, doi:10.1038/364701a0.

977 Mashayek, A., R. Ferrari, S. Merrifield, J. R. Ledwell, L. St Laurent, and A. N. Garabato, 2017:
978 Topographic enhancement of vertical turbulent mixing in the Southern Ocean. *Nature Commu-*
979 *nications*, **8**, 14 197, doi:10.1038/ncomms14197.

980 McDougall, T. J., and R. Ferrari, 2017: Abyssal upwelling and downwelling driven by near-
981 boundary mixing. *J. Phys. Oceanogr.*, **47 (2)**, 261–283, doi:10.1175/JPO-D-16-0082.1.

982 McPhee-Shaw, E., 2006: Boundary-interior exchange: Reviewing the idea that internal-wave mix-
983 ing enhances lateral dispersal near continental margins. *Deep-Sea Res. II*, **53 (1)**, 42 – 59, doi:
984 10.1016/j.dsr2.2005.10.018.

985 Moré, J. J., 1978: The Levenberg-Marquardt algorithm: Implementation and theory. *Numerical*
986 *analysis*, Springer, 105–116.

987 Munk, W. H., 1966: Abyssal recipes. *Deep Sea Research and Oceanographic Abstracts*, **13 (4)**,
988 707 – 730, doi:10.1016/0011-7471(66)90602-4.

989 Phillips, O., 1970: On flows induced by diffusion in a stably stratified fluid. *Deep Sea Research*
990 *and Oceanographic Abstracts*, **17 (3)**, 435–443, doi:10.1016/0011-7471(70)90058-6.

991 Phillips, O., J.-H. Shyu, and H. Salmun, 1986: An experiment on boundary mixing: Mean circu-
992 lation and transport rates. *J. Fluid Mech.*, **173**, 473–499, doi:10.1017/S0022112086001234.

993 Polzin, K. L., J. M. Toole, J. R. Ledwell, and R. W. Schmitt, 1997: Spatial variability of turbulent
994 mixing in the abyssal ocean. *Science*, **276 (5309)**, 93–96, doi:10.1126/science.276.5309.93.

995 Redi, M. H., 1982: Oceanic isopycnal mixing by coordinate rotation. *J. Phys. Oceanogr.*, **12 (10)**,
996 1154–1158, doi:10.1175/1520-0485(1982)012⟨1154:OIMBCR⟩2.0.CO;2.

997 Rhines, P. B., and W. R. Young, 1982: Homogenization of potential vorticity in planetary gyres.
998 *J. Fluid Mech.*, **122**, 347–367.

Saffman, P. G., 1962: The effect of wind shear on horizontal spread from an instantaneous ground source. *Q. J. Roy. Meteorol. Soc.*, **88 (378)**, 382–393, doi:10.1002/qj.49708837803.

St. Laurent, L., A. C. Naveira Garabato, J. R. Ledwell, A. M. Thurnherr, J. M. Toole, and A. J. Watson, 2012: Turbulence and diapycnal mixing in Drake Passage. *J. Phys. Oceanogr.*, **42 (12)**, 2143–2152, doi:10.1175/JPO-D-12-027.1.

St. Laurent, L., J. Toole, and G. A. Schmidt, 2001: Buoyancy forcing by turbulence above rough topography in the abyssal brazil basin. *J. Phys. Oceanogr.*, **31 (12)**, 3476–3495, doi:10.1175/1520-0485(2001)031⟨3476:BFBTAR⟩2.0.CO;2.

Thorpe, S. A., 1987: Current and temperature variability on the continental slope. *Philosophical Transactions of the Royal Society of London A: Mathematical, Physical and Engineering Sciences*, **323 (1574)**, 471–517, doi:10.1098/rsta.1987.0100.

Toole, J. M., R. W. Schmitt, and K. L. Polzin, 1994: Estimates of diapycnal mixing in the abyssal ocean. *Science*, **264 (5162)**, 1120–1123, doi:10.1126/science.264.5162.1120.

Voet, G., J. B. Girton, M. H. Alford, G. S. Carter, J. M. Klymak, and J. B. Mickett, 2015: Pathways, volume transport, and mixing of abyssal water in the samoan passage. *J. Phys. Oceanogr.*, **45 (2)**, 562–588, doi:10.1175/JPO-D-14-0096.1.

Wain, D. J., and C. R. Rehmann, 2010: Transport by an intrusion generated by boundary mixing in a lake. *Water Resources Research*, **46 (8)**, doi:10.1029/2009WR008391, w08517.

Waterhouse, A. F., and Coauthors, 2014: Global patterns of diapycnal mixing from measurements of the turbulent dissipation rate. *J. Phys. Oceanogr.*, **44 (7)**, 1854–1872, doi:10.1175/JPO-D-13-0104.1.

Watson, A. J., and J. R. Ledwell, 2000: Oceanographic tracer release experiments using sulphur hexafluoride. *J. Geophys. Res.*, **105 (C6)**, 14 325–14 337, doi:10.1029/1999JC900272.

Watson, A. J., J. R. Ledwell, M.-J. Messias, B. A. King, N. Mackay, M. P. Meredith, B. Mills, and A. C. Naveira Garabato, 2013: Rapid cross-density ocean mixing at mid-depths in the Drake Passage measured by tracer release. *Nature*, **501**, 408–, doi:10.1038/nature12432.

Wenegrat, J. O., J. Callies, and L. N. Thomas, 2018: Submesoscale baroclinic instability in the bottom boundary layer. *J. Phys. Oceanogr.*, **48**, 2571–2592, doi:10.1175/JPO-D-17-0264.1.

Winters, K. B., 2015: Tidally driven mixing and dissipation in the stratified boundary layer above steep submarine topography. *Geophys. Res. Lett.*, **42 (17)**, 7123–7130, doi:10.1002/2015GL064676.

Wüest, A., D. van Senden, J. Imberger, G. Piepke, and M. Gloor, 1996: Comparison of diapycnal diffusivity measured by tracer and microstructure techniques. *Dynam. Atmos. Ocean*, **24 (1)**, 27 – 39, doi:10.1016/0377-0265(95)00408-4.

Wunsch, C., 1970: On oceanic boundary mixing. *Deep Sea Research and Oceanographic Abstracts*, **17 (2)**, 293 – 301, doi:10.1016/0011-7471(70)90022-7.

Young, W., P. Rhines, and C. Garrett, 1982: Shear-flow dispersion, internal waves and horizontal mixing in the ocean. *J. Phys. Oceanogr.*, **12 (6)**, 515–527, doi:10.1175/1520-0485(1982)012⟨0515:SFDIWA⟩2.0.CO;2.

Zamani, K., and F. A. Bombardelli, 2014: Analytical solutions of nonlinear and variable-parameter transport equations for verification of numerical solvers. *Environmental Fluid Mechanics*, **14 (4)**, 711–742, doi:10.1007/s10652-013-9325-0.

# LIST OF FIGURES

**Fig. 6.** The evolution of tracer patches released (a-c) $z_0 = 3d/4 = 375$m and (d-f) $z_0 = d/8 = 62.5$m above the bottom (open white circle) with a bottom-intensified isotropic diffusivity and no along-isopycnal diffusivity. The position of the tracer center-of-mass $(\mu_y, \mu_z)$ is shown with a closed white circle and the center-of-mass on the boundary is shown with a cross. . . . . 57

**Fig. 7.** Buoyancy space tracer behavior for the two runs considered in Fig. 6, where the tracer is released $z_0 = 3d/4 = 375$m (orange lines) and $z_0 = d/8 = 62.5$m (blue lines) above the bottom. (a) The tracer distribution as a function of buoyancy at days 0, 192 and 800. (b) Time series of the center of mass $\mu_b$ (solid lines), the contribution of the diffusivity gradient to center-of-mass trends (dotted lines) and the contribution of BBL advection to center-of-mass trends (dashed lines). (c) Time series of the bulk diffusivity (solid lines), in-situ diffusivity (dashed lines) and the contribution of the diffusivity gradient to the bulk diffusivity (dotted lines). . . . . 58

**Fig. 8.** The change in the tracer center-of-mass in buoyancy space from its initial buoyancy $\Delta\mu_b = \mu_b(t) - \mu_b(0)$ at day 800 as a function of the initial release height of the tracer above the bottom boundary. . . . . 59

**Fig. 9.** (a-c) The evolution of tracer patches released $z_0 = d/2 = 250$m above the bottom (open white circle) as for Fig. 4d-f (with different axis limits) with a slope of $1/400$, $d = 500$m and $SPr_{u0}^{-1} = 0$. (d-f) As for a-c except with a slope of $1/100$. (g-i) As for a-c except with the vertical stratification in the SML reduced by a factor of three through the choice $SPr_{u0}^{-1} = 2$. (j-l) As for a-c except with the diffusivity decay scale reduced to $d = 200$m. Plots are shown at day (a,d,g,j) 400, (b,e,h,k) 800 and (c,f,i,l) 1600. The position of the tracer center-of-mass $(\mu_y, \mu_z)$ is shown with a solid white circle and the center-of-mass on the boundary is shown with a cross. . . . . 60

**Fig. 10.** Buoyancy space tracer behavior for the runs considered in Fig. 9a-c and Fig. 9j-l where the tracer is released 250m above the bottom and the vertical decay scale of the diffusivity is $d = 500$m (orange lines) and $d = 200$m (blue lines). (a) The tracer distribution as a function of buoyancy at days 0, 192 and 1600. (b) Time series of the center of mass $\mu_b$ (solid lines), the contribution of the diffusivity gradient to center-of-mass trends (dotted lines) and the contribution of BBL advection to center-of-mass trends (dashed lines). (c) Time series of the bulk diffusivity (solid lines), in-situ diffusivity (dashed lines) and the contribution of the diffusivity gradient to the bulk diffusivity (dotted lines). . . . . 61

**Fig. 11.** The evolution of tracer patches released $z_0 = d/2 = 250$m above the bottom (open white circle) with an exponential diffusivity for two values of along-isopycnal diffusivity (a-c) $A_H = 10\text{m}^2\text{s}^{-1}$ and (d-f) $A_H = 100\text{m}^2\text{s}^{-1}$ at day (a,d) 400 , (b,e) 800 and (c,f) 1600. The position of the tracer center-of-mass $(\mu_y, \mu_z)$ is shown with a solid white circle and the center-of-mass on the boundary is shown with a cross. . . . . 62

**Fig. 12.** Buoyancy-space tracer behavior for the two runs considered in Fig. 11 with along-isopycnal diffusivity $A_H = 10\text{m}^2\text{s}^{-1}$ (orange lines) and $A_H = 100\text{m}^2\text{s}^{-1}$ (blue lines). (a) The tracer distribution as a function of buoyancy at days 0, 192 and 1600. (b) Time series of the center of mass $\mu_b$ (solid lines), the contribution of the diffusivity gradient to center-of-mass trends (dotted lines) and the contribution of BBL advection to center-of-mass trends (dashed lines). (c) Time series of the instantaneous bulk diffusivity (solid lines), in-situ diffusivity (dashed lines) and the contribution of the diffusivity gradient to the bulk diffusivity (dotted lines). . . . 63

**Fig. 13.** A summary of the time-averaged (or cumulative) diffusivity between days 0 and 800 from all the point-release experiments with a slope of $1/400$, bottom-intensified mixing and a release

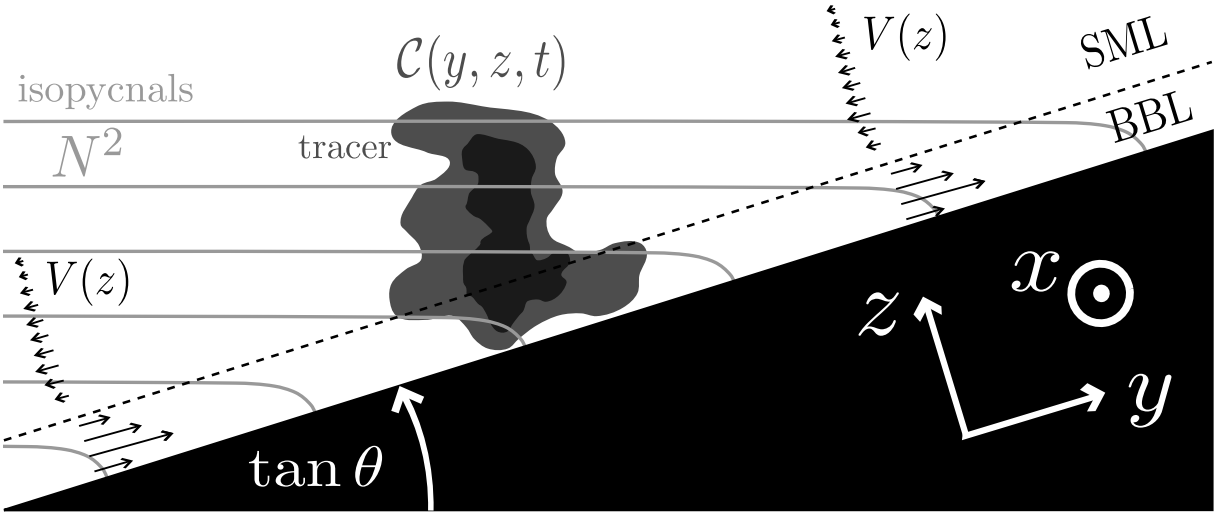


FIG. 1. A schematic illustrating the two-dimensional slope-normal coordinate system used in this article. The boundary has a constant slope of $\tan\theta$. The coordinate system is aligned with the slope such that $z$ is normal to the slope, $y$ points up the slope and $x$ is along-slope. The density field is characterized by a constant stratification $N^2$ within the SML, while isopycnals slope down within the weakly stratified BBL. One-dimensional boundary layer theory yields an upslope velocity profile $V(z)$ that is characterized by strong upwelling across isopycnals in the BBL with weaker downwelling across isopycnals in the SML. The tracer $\mathcal{C}$ is released at some point in the domain and evolves in the two spatial dimensions $y$, $z$ and in time $t$.

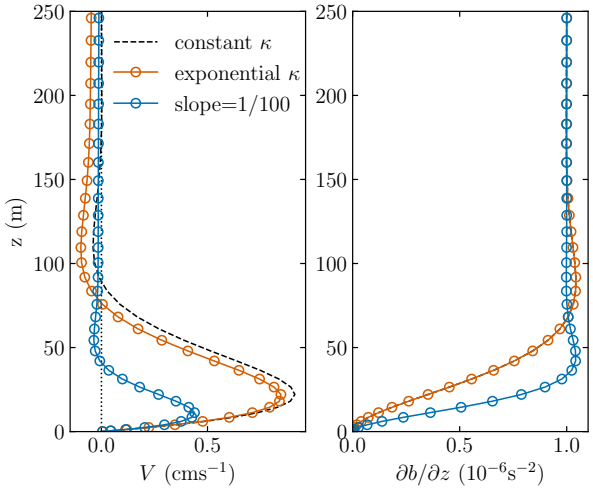


FIG. 2. Upslope velocity $V$ (left) and buoyancy frequency (right) $\frac{\partial b}{\partial z}$ from the approximate analytic solution [Eq. (11)] for a constant diffusivity $\kappa = \kappa_0$ (dashed black) and an exponentially-decaying isotropic diffusivity $\kappa = \kappa_\infty + (\kappa_0 - \kappa_\infty)e^{-z/d}$ (colored). Parameters are $N^2 = 10^{-6}\text{s}^{-2}$, $\kappa_0 = 10^{-3}\text{m}^2\text{s}^{-1}$, $\kappa_\infty = 10^{-5}\text{m}^2\text{s}^{-1}$ and $d = 500\text{m}$. The orange curves and the constant $\kappa$ case use a slope of $\tan\theta = 1/400$, where the BBL width $q_0^{-1} = 28.3\text{m}$, while the blue curves use a slope of $1/100$, where $q_0^{-1} = 14.1\text{m}$. Stratification in the constant $\kappa$ case is identical to that in the exponential case. The open circles indicate the effective vertical grid resolution of the Dedalus simulations for 192 Chebyshev modes.

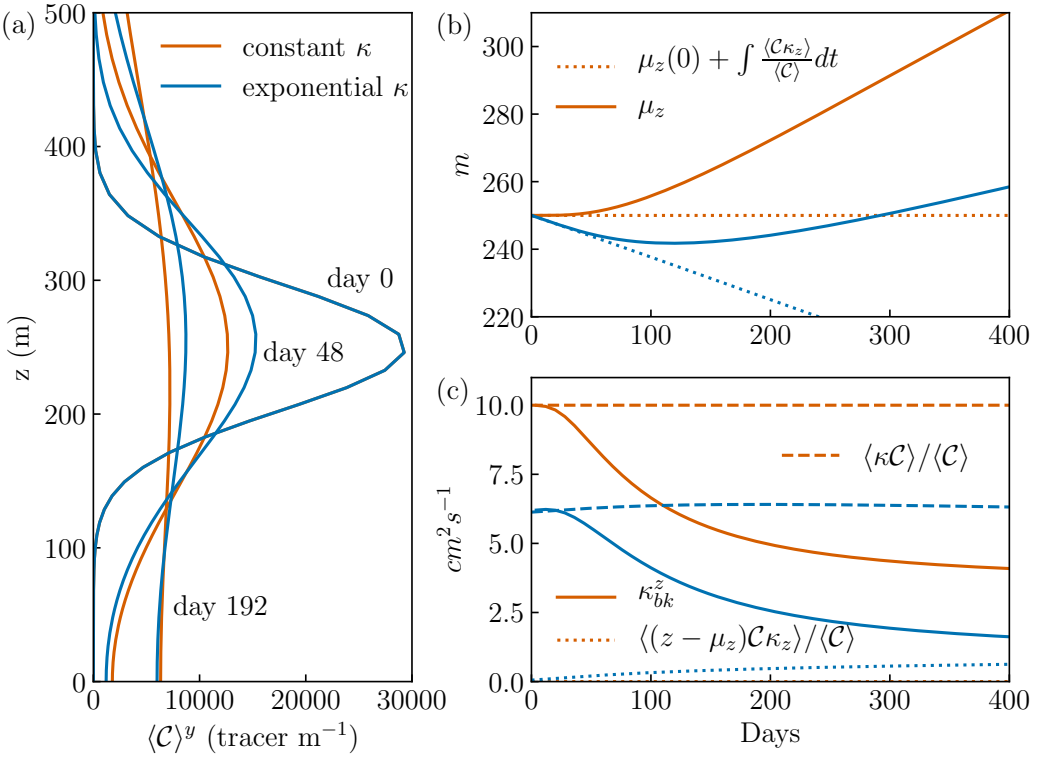


FIG. 3. Behavior of the tracer in $z$ for a constant diffusivity $\kappa = \kappa_0$ (orange lines) and an exponential diffusivity (blue lines). (a) The tracer distribution as a function of $z$ integrated in $y$, $\langle\mathcal{C}\rangle^y$, at days 0, 48 and 192. (b) Time series of the center of mass $\mu_z$ (solid lines) and the time-integrated contribution of the diffusivity gradient to center-of-mass changes (dotted lines, obtained by time-integrating the second term on the RHS of Eq. (37), and adding the initial center-of-mass $\mu_z(0)$). Note that the contribution of the boundary term (first term on RHS of Eq. (37)) accounts for the increase in $\mu_z$ beyond the effect of the diffusivity gradient. (c) The bulk diffusivity $\kappa^z_{bk}$ from the tracer variance (solid lines), the in-situ diffusivity (dashed lines) and the contribution to $\kappa^z_{bk}$ from the diffusivity gradient (dotted lines). Note again that the boundary term (second term in Eq. (40)) is not shown and accounts for the down-turn in $\kappa^z_{bk}$.

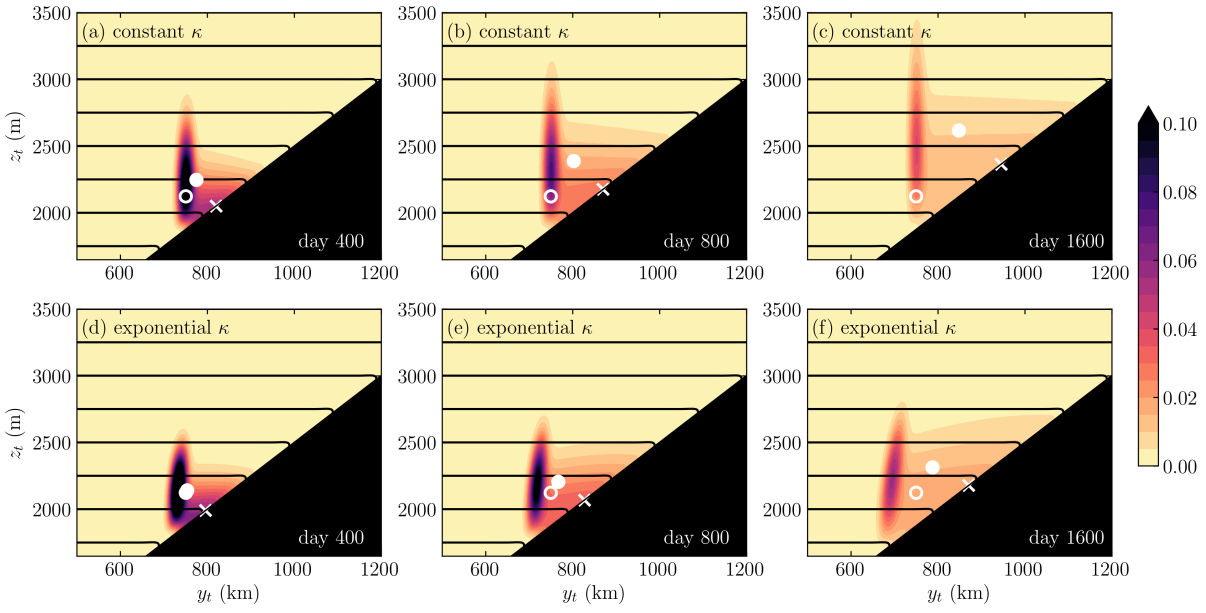


FIG. 4. The evolution of a tracer patch released $z_0 = d/2 = 250$m above the bottom (open white circle) with (a-c) a constant diffusivity and (d-f) a bottom-intensified diffusivity. Tracer concentrations are shown at days (a,d) 400 , (b,e) 800 and (c,f) 1600. The position of the tracer center-of-mass $(\mu_y, \mu_z)$ is shown with a solid circle and the position of the center-of-mass of tracer located only on the boundary is shown with a cross. Note that the aspect ratio is strongly exaggerated.

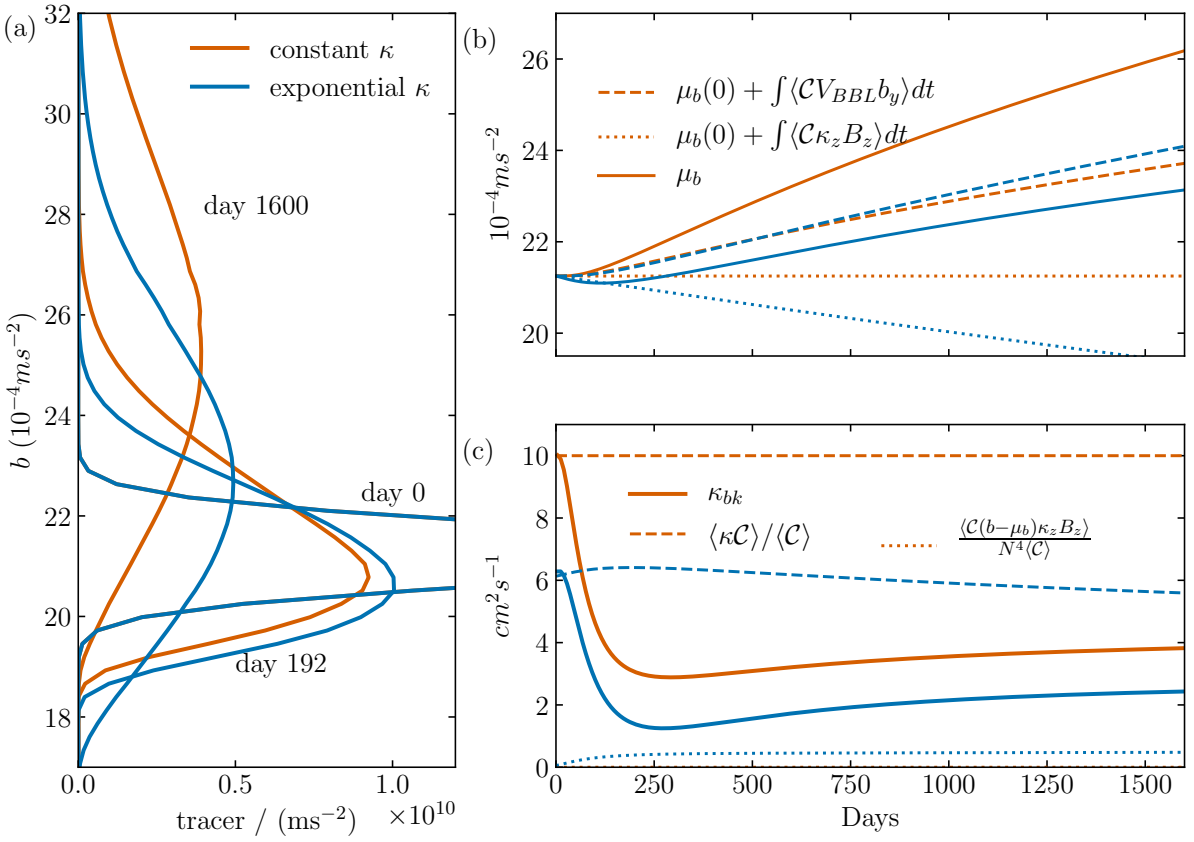


1195 FIG. 5. Buoyancy space tracer behavior for the two runs considered in Fig. 4 with constant diffusivity (orange
1196 lines) and exponential diffusivity (blue lines). (a) The tracer distribution as a function of $b$ at days 0, 192 and
1197 1600. (b) Time series of the center of mass $\mu_b$ (solid lines), the contribution of the diffusivity gradient to center-
1198 of-mass trends (dotted lines) and the contribution of BBL advection to center-of-mass trends (dashed lines).
1199 As discussed in Section 6a, advection and diffusion each contribute half of the total trend, with the boundary
1200 term and BBL advection also making equal contributions. (c) Time series of the bulk diffusivity (solid lines),
1201 in-situ diffusivity (dashed lines) and the contribution of the diffusivity gradient to the bulk diffusivity (dotted
1202 line). As discussed in Section 6d, the influence of SML advection is equivalent to the diffusivity gradient effect
1203 (dotted line), while BBL advection and the boundary effect account, in equal parts, for the reduction in the bulk
1204 diffusivity well below the in-situ diffusivity.

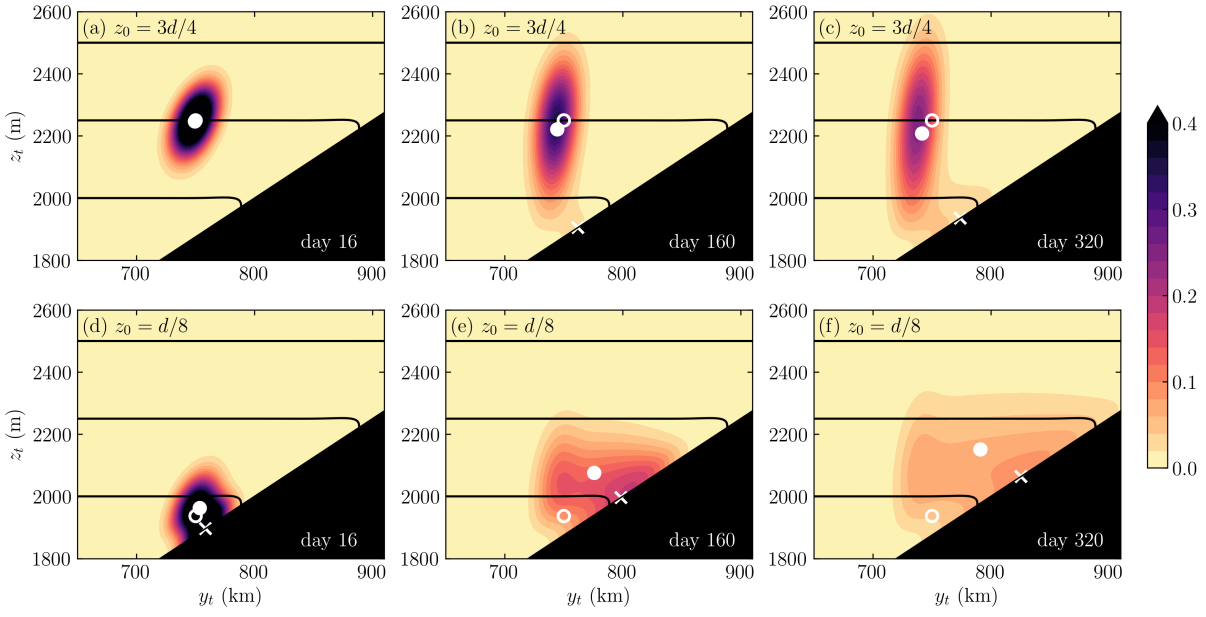


FIG. 6. The evolution of tracer patches released (a-c) $z_0 = 3d/4 = 375$m and (d-f) $z_0 = d/8 = 62.5$m above the bottom (open white circle) with a bottom-intensified isotropic diffusivity and no along-isopycnal diffusivity. The position of the tracer center-of-mass $(\mu_y, \mu_z)$ is shown with a closed white circle and the center-of-mass on the boundary is shown with a cross.

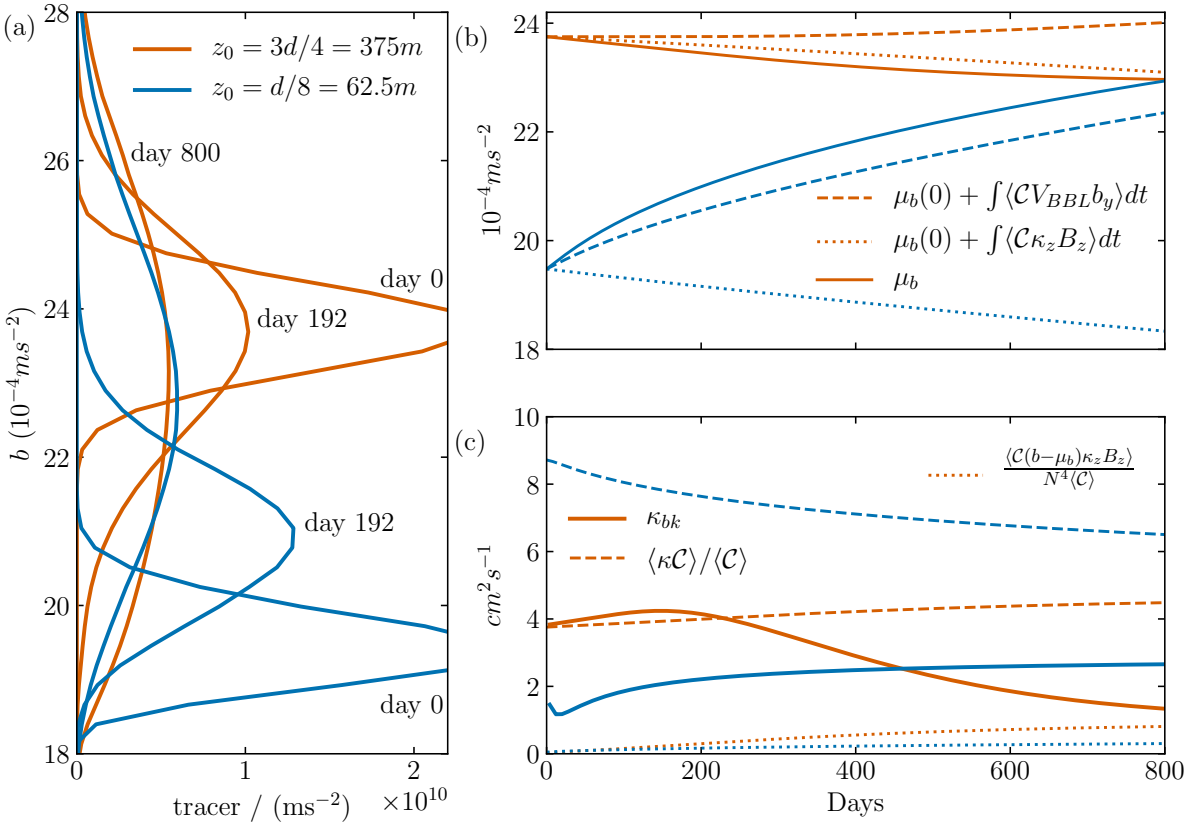


FIG. 7. Buoyancy space tracer behavior for the two runs considered in Fig. 6, where the tracer is released $z_0 = 3d/4 = 375$m (orange lines) and $z_0 = d/8 = 62.5$m (blue lines) above the bottom. (a) The tracer distribution as a function of buoyancy at days 0, 192 and 800. (b) Time series of the center of mass $\mu_b$ (solid lines), the contribution of the diffusivity gradient to center-of-mass trends (dotted lines) and the contribution of BBL advection to center-of-mass trends (dashed lines). (c) Time series of the bulk diffusivity (solid lines), in-situ diffusivity (dashed lines) and the contribution of the diffusivity gradient to the bulk diffusivity (dotted lines).

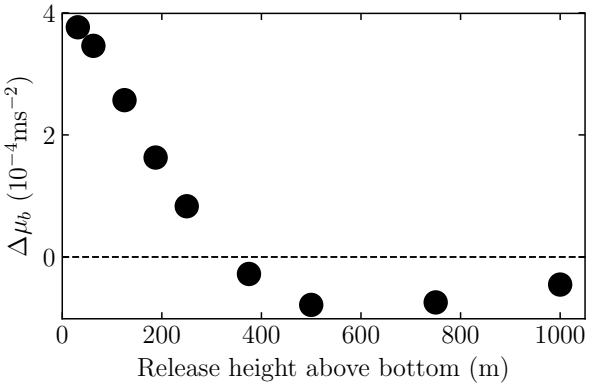


FIG. 8. The change in the tracer center-of-mass in buoyancy space from its initial buoyancy $\Delta\mu_b = \mu_b(t) - \mu_b(0)$ at day 800 as a function of the initial release height of the tracer above the bottom boundary.

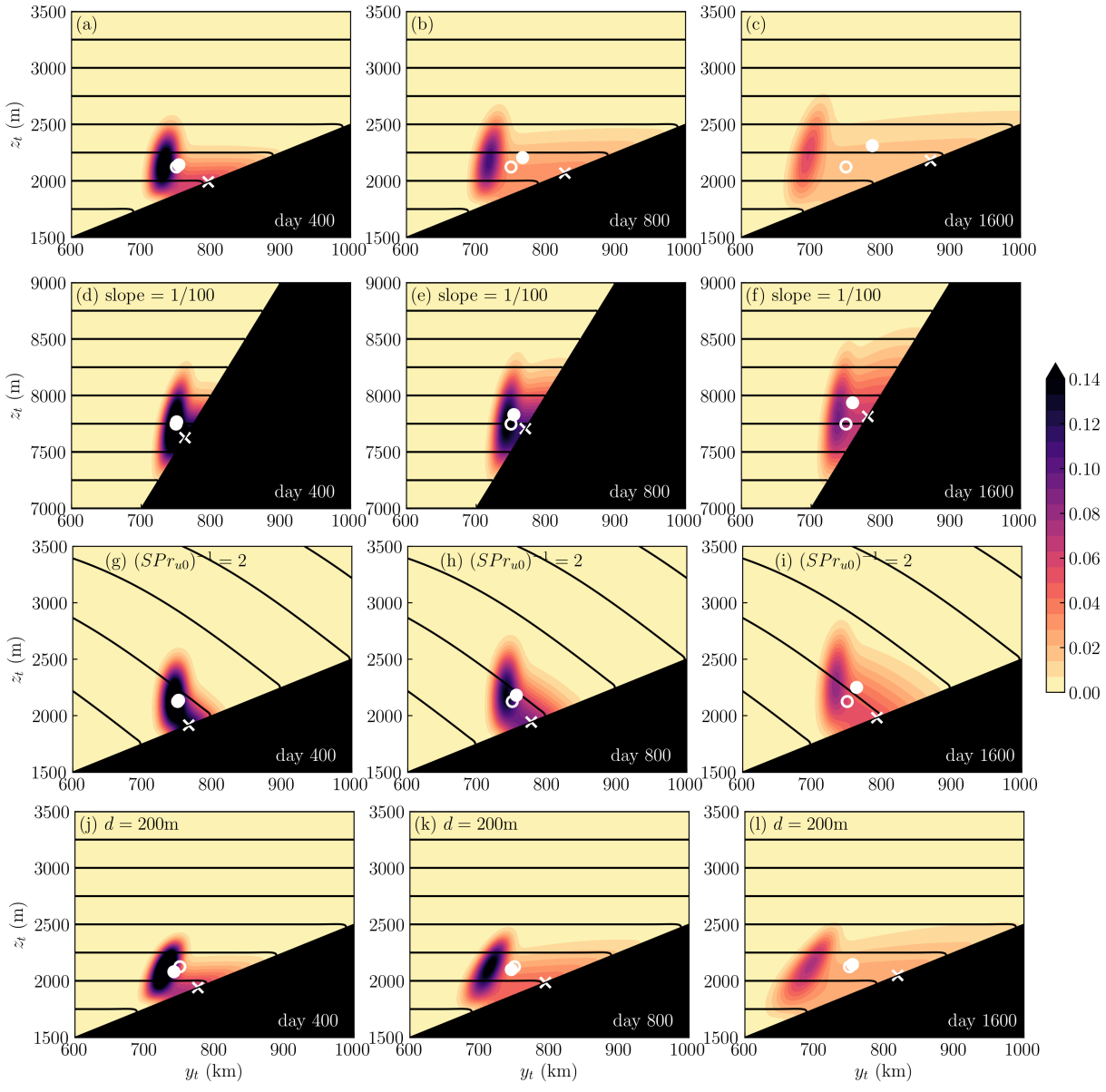


FIG. 9. (a-c) The evolution of tracer patches released $z_0 = d/2 = 250$m above the bottom (open white circle) as for Fig. 4d-f (with different axis limits) with a slope of $1/400$, $d = 500$m and $SPr_{u0}^{-1} = 0$. (d-f) As for a-c except with a slope of $1/100$. (g-i) As for a-c except with the vertical stratification in the SML reduced by a factor of three through the choice $SPr_{u0}^{-1} = 2$. (j-l) As for a-c except with the diffusivity decay scale reduced to $d = 200$m. Plots are shown at day (a,d,g,j) 400, (b,e,h,k) 800 and (c,f,i,l) 1600. The position of the tracer center-of-mass $(\mu_y, \mu_z)$ is shown with a solid white circle and the center-of-mass on the boundary is shown with a cross.

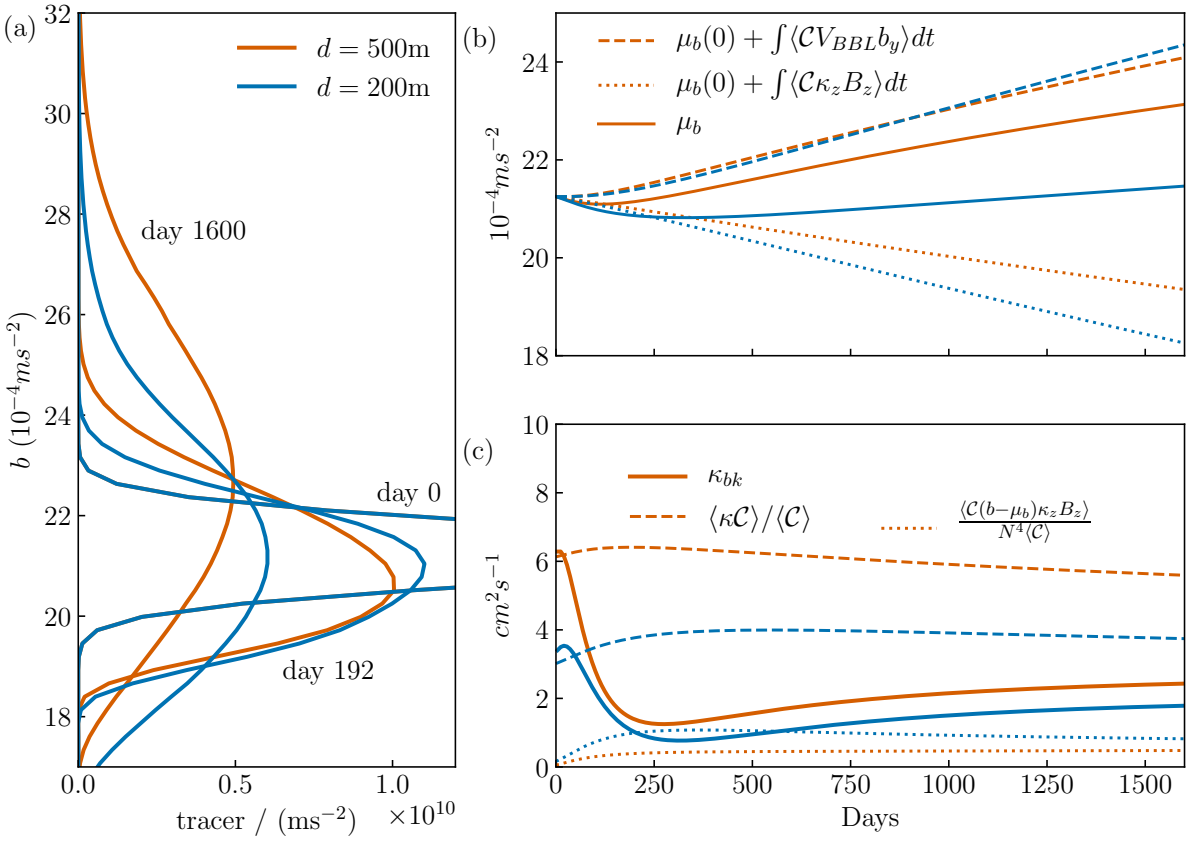


1224 FIG. 10. Buoyancy space tracer behavior for the runs considered in Fig. 9a-c and Fig. 9j-l where the tracer is
1225 released 250m above the bottom and the vertical decay scale of the diffusivity is $d = 500$m (orange lines) and
1226 $d = 200$m (blue lines). (a) The tracer distribution as a function of buoyancy at days 0, 192 and 1600. (b) Time
1227 series of the center of mass $\mu_b$ (solid lines), the contribution of the diffusivity gradient to center-of-mass trends
1228 (dotted lines) and the contribution of BBL advection to center-of-mass trends (dashed lines). (c) Time series of
1229 the bulk diffusivity (solid lines), in-situ diffusivity (dashed lines) and the contribution of the diffusivity gradient
1230 to the bulk diffusivity (dotted lines).

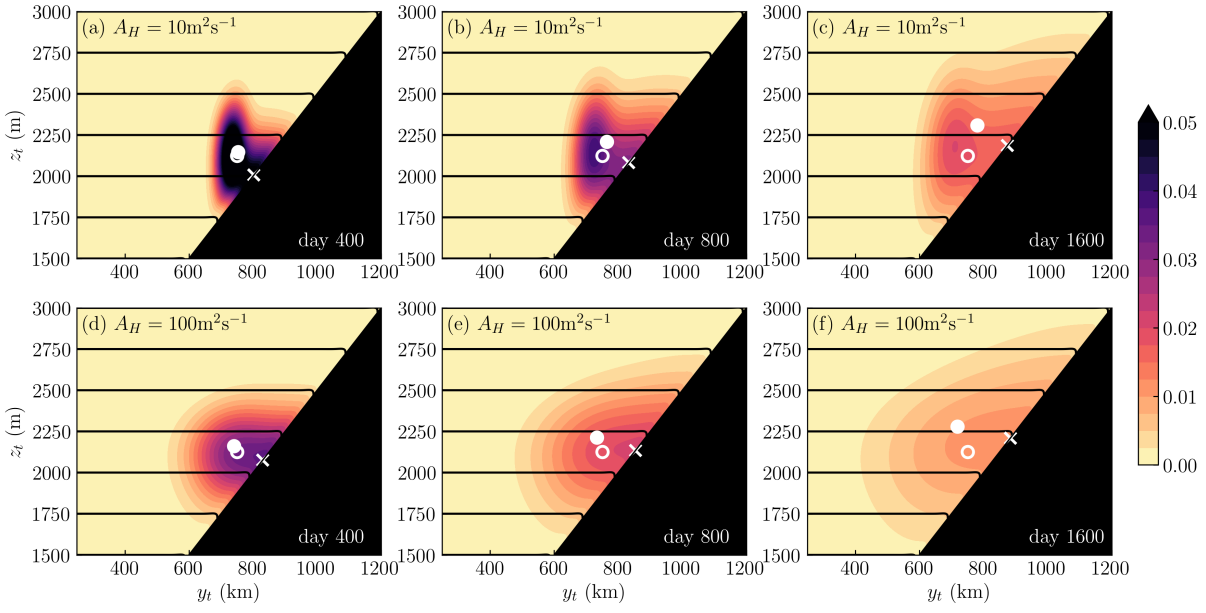


FIG. 11. The evolution of tracer patches released $z_0 = d/2 = 250$m above the bottom (open white circle) with an exponential diffusivity for two values of along-isopycnal diffusivity (a-c) $A_H = 10\mathrm{m}^2\mathrm{s}^{-1}$ and (d-f) $A_H = 100\mathrm{m}^2\mathrm{s}^{-1}$ at day (a,d) 400 , (b,e) 800 and (c,f) 1600. The position of the tracer center-of-mass $(\mu_y, \mu_z)$ is shown with a solid white circle and the center-of-mass on the boundary is shown with a cross.

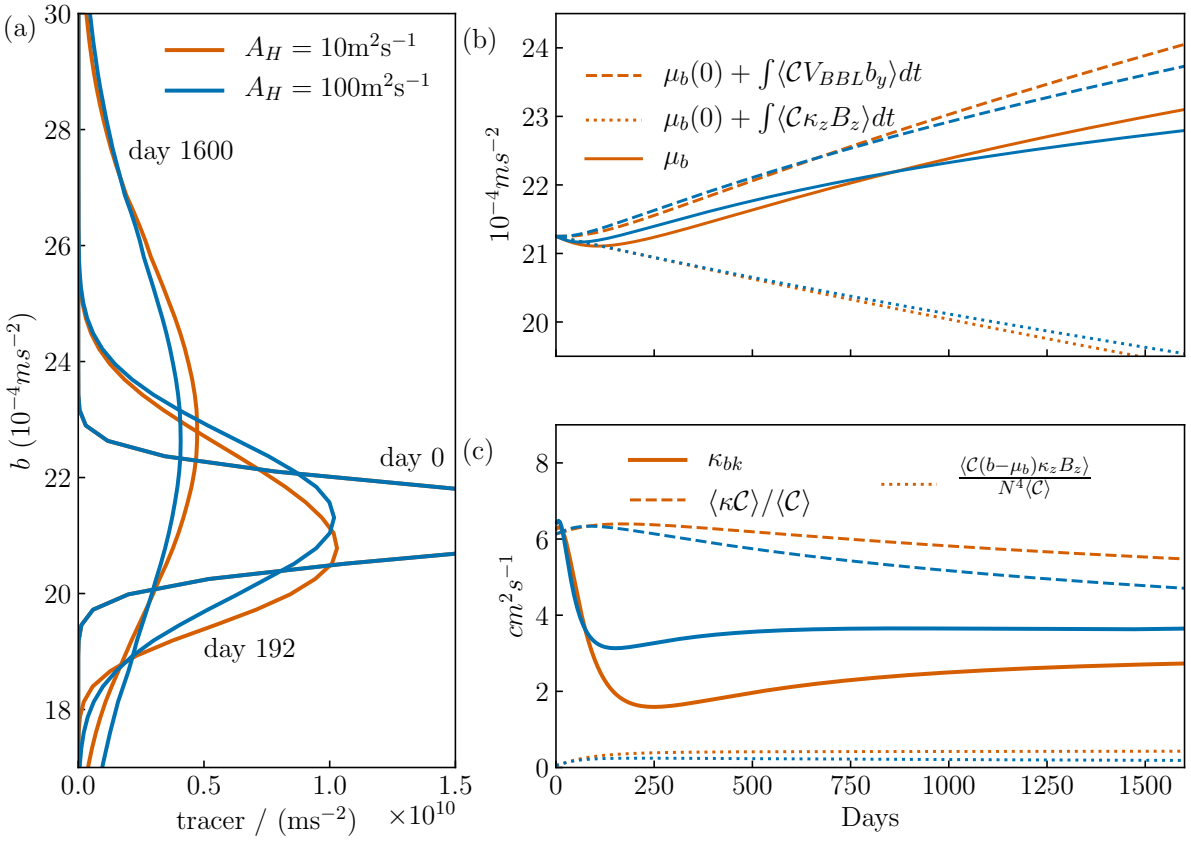


FIG. 12. Buoyancy-space tracer behavior for the two runs considered in Fig. 11 with along-isopycnal diffusivity $A_H = 10\mathrm{m}^2\mathrm{s}^{-1}$ (orange lines) and $A_H = 100\mathrm{m}^2\mathrm{s}^{-1}$ (blue lines). (a) The tracer distribution as a function of buoyancy at days 0, 192 and 1600. (b) Time series of the center of mass $\mu_b$ (solid lines), the contribution of the diffusivity gradient to center-of-mass trends (dotted lines) and the contribution of BBL advection to center-of-mass trends (dashed lines). (c) Time series of the instantaneous bulk diffusivity (solid lines), in-situ diffusivity (dashed lines) and the contribution of the diffusivity gradient to the bulk diffusivity (dotted lines).

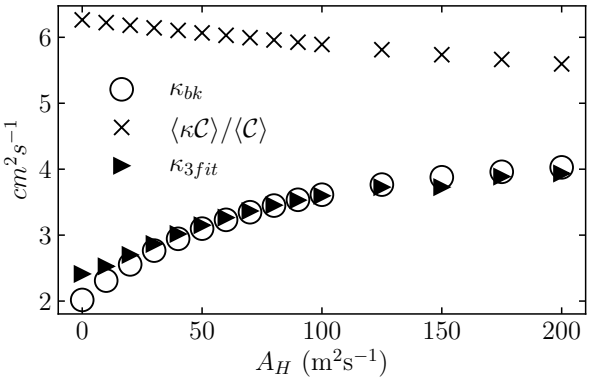


FIG. 13. A summary of the time-averaged (or cumulative) diffusivity between days 0 and 800 from all the point-release experiments with a slope of $1/400$, bottom-intensified mixing and a release point at $z_0 = d/2$. Shown are the time-averaged bulk (open circles) and in-situ (crosses) diffusivities as a function of the along-isopycnal diffusivity $A_H$. Also shown (black triangles) is the diffusivity estimated from a three-parameter least-squares fit to a 1D advection-diffusion equation (Ledwell and Watson 1991; Ledwell 1998, see Appendix B).

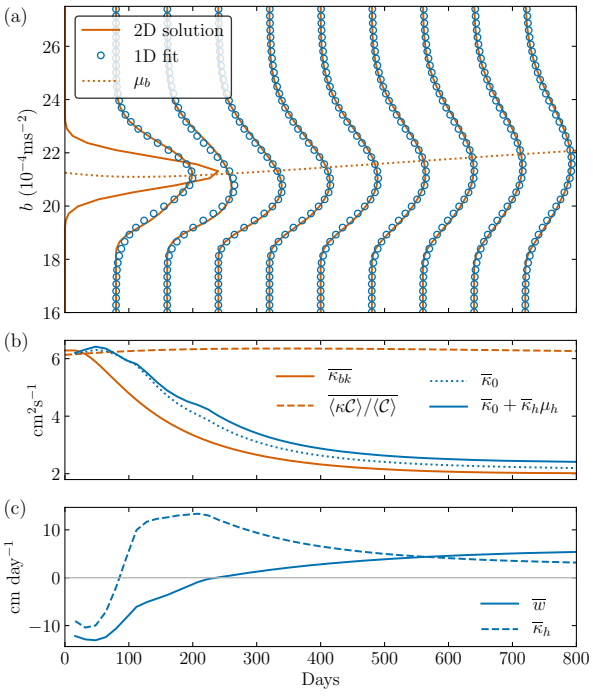


Fig. A1. (a) Evolution of the tracer buoyancy profiles for the exponential isotropic diffusivity two-dimensional case shown in Fig. 5 (solid lines) and the center-of-mass time series (dotted lines). The open circles are profiles from a three-parameter least-squares fit to a one-dimensional advection-diffusion equation [Eq. (72)]. (b) Time series of the time-averaged bulk diffusivity (solid orange line), the in-situ diffusivity (dashed orange line) and the diffusivities estimated from the three-parameter least-squares fit at $h = 0$ (dotted blue line) and at $h = \mu_h$ (solid blue line). (c) Time series of the diffusivity gradient (dashed line) and diapycnal velocity (solid line) from the three-parameter fit.

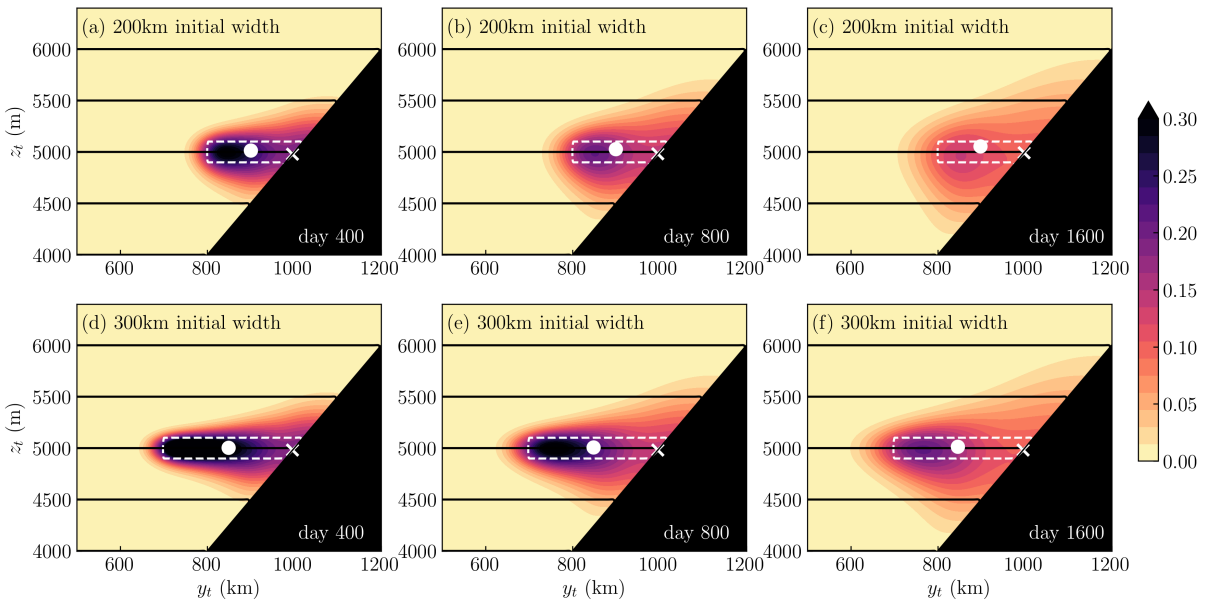


Fig. A2. Tracer distributions for experiments where the initial tracer distribution is a narrow Gaussian centered about a particular buoyancy (whose initial extent is indicated by the dashed white box), the along-isopycnal diffusivity is $A_H = 10\text{m}^2\text{s}^{-1}$ and the slope is $1/200$. The initial width of the tracer distribution extends out to a distance (a-c) $2d = 1000$m above the bottom, or a horizontal distance of 200km from the boundary and (d-f) $3d = 1500$m above the bottom, or a horizontal distance of 300km from the boundary. Distributions are shown at day (a,d) 400, (b,e) 800 and (c,f) 1600. The position of the tracer center-of-mass $(\mu_y, \mu_z)$ is shown with a white circle and the center-of-mass on the boundary is shown with a cross.

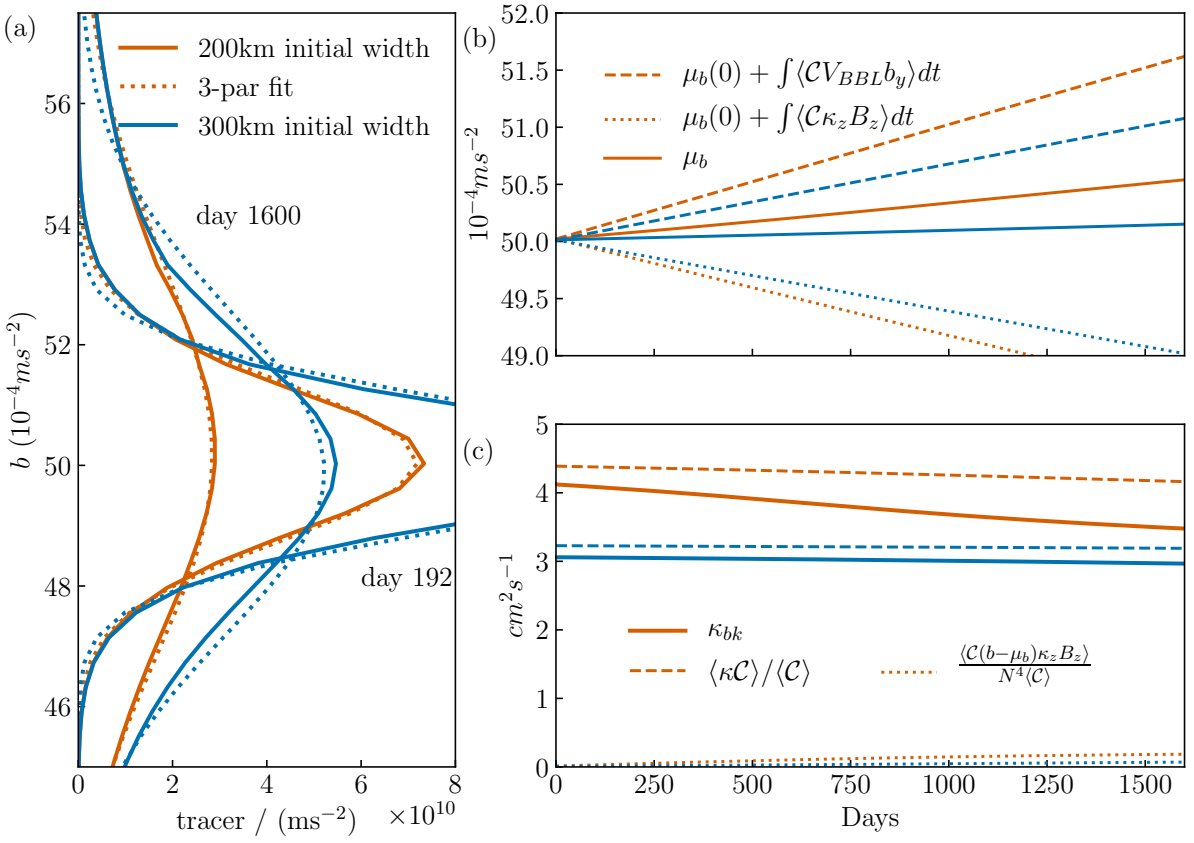


Fig. A3. Buoyancy-space tracer behavior for the cases considered in Fig. A2. (a) The tracer distribution as a function of buoyancy at days 192 and 1600. Also shown are the predicted tracer distributions from the one-dimensional least-squares fit discussed in Appendix B (dotted lines). (b) Time series of the center of mass $\mu_b$ (solid lines), the contribution of the diffusivity gradient to center-of-mass trends (dotted lines) and the contribution of BBL advection to center-of-mass trends (dashed lines). (c) Time series of the instantaneous bulk diffusivity (solid lines), in-situ diffusivity (dashed lines) and the contribution of the diffusivity gradient to the bulk diffusivity (dotted lines).

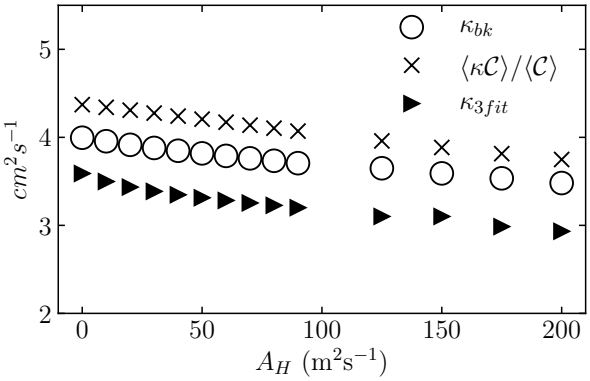


Fig. A4. A summary of the time-averaged (or cumulative) diffusivity between days 0 and 800 from all the layer-release experiments with a slope of $1/200$ and where the layer has an initial width of 200km, or extends out to a distance of $2d = 1000$m above the bottom. Shown are the time-averaged bulk (open circles) and in-situ (crosses) diffusivities as a function of the along-isopycnal diffusivity $A_H$. Also shown (black triangles) is the diffusivity estimated from a three-parameter least-squares fit to a 1D advection-diffusion equation (Ledwell and Watson 1991; Ledwell 1998, see Appendix B).